FATIGUE BEHAVIOR OF CORROSION NOTCHED WEATHERING STEEL SAMPLES

by

Di Chen

A Thesis Submitted to the Faculty of

The College of Engineering and Computer Science

in Partial Fulfillment of the Requirements for the Degree of

Master of Science

Florida Atlantic University

Boca Raton, Florida

May 2014

FATIGUE BEHAVIOR OF CORROSION NOTCHED

WEATHERING STEEL SAMPLES

by

Di Chen

This thesis was prepared under the direction of the candidate's thesis advisor, Dr. Richard Granata, Department of Ocean and Mechanical Engineering, and has been approved by the members of his supervisory committee. It was submitted to the faculty of the College of Engineering and Computer Science and was accepted in partial fulfillment of the requirements for the degree of Master of Science.

SUPERVISORY COMMITTEE:

Richard Granata, Ph.D.
Thesis Advisor

Hassan Mahfuz, Ph.D.

Francisco Presuel-Moreno, Ph.D.

Javad Hashemi, Ph.D.
Chair, Department of Ocean and Mechanical Engineering

Mohammad Ilyas, Ph.D.
Dean, College of Engineering and Computer Science

Deborah L. Floyd, Ed.D.
Interim Dean, Graduate College

April 11, 2014
Date

ACKNOWLEDGEMENTS

The author wishes to express his thanks to Dr. Richard Granata for providing sponsorship to conduct the study. The author is also grateful to Dr. Hassan Mahfuz and Dr. Francisco Presuel-Moreno for providing guidance and advices. The efforts of the support personnel are also greatly appreciated. Partial support of the Florida Department of Transportation under contract BDK79 TWO 977-06 “Environmental Suitability of Weathering Steel Structures in Florida – Material Selection”, FAU-645044, is gratefully acknowledged. The opinions, findings and conclusions expressed in this publication are those of the author and not necessarily those of the Florida Department of Transportation or the U.S. Department of Transportation.

ABSTRACT

Author: Di CHEN

Title: Fatigue Behavior of Corrosion Notched Weathering Steel Samples

Institution: Florida Atlantic University

Advisor: Dr. Richard Granata

Degree: Master of Science

Year: 2014

Weathering steel has been a primary construction material for bridges in the United States. Notches caused by corrosion are observed on the flange of steel I-beams. These notches reduce the cross section area of the structure and are threats to bridge safety. A606-04 Type 4 cold rolled weathering steel samples were studied in this thesis to understand the effect of notches that caused by corrosion. Weathering steel samples were in the shape of plates, which simulated flange of I-beams. The plate samples were notched across their surfaces by applying electrical current through an electrochemical circuit composed of an anode, a cathode and electrolyte. Sixteen samples were notched and cut into appropriate shape for fatigue testing. S-N (Stress-Number of cycles to failure) diagram established from fatigue data indicated that the fatigue strength decreased below AASHTO category B. Weibull analysis was also performed to understand the reliability distribution.

FATIGUE BEHAVIOR OF CORROSION NOTCHED

WEATHERING STEEL SAMPLES

LIST OF FIGURES

LIST OF TABLES

1. INTRODUCTION

The first goal of this thesis is to develop an efficient notch creation method that simulates in a short amount of time the corrosion process on the flange of steel I-beams as observed in Fig.1. The second goal is to study how the developed notch would affect fatigue behavior of weathering steel structures. This thesis study will provide bridge structural designers a method for studying fatigue on notched weathering steel (WS) I-beams or plates.

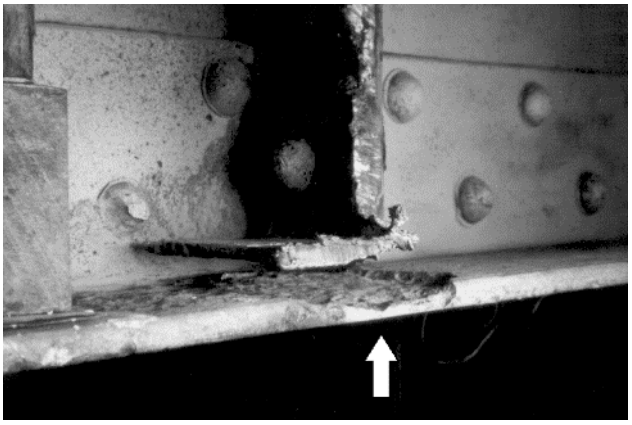

Figure 1 Corrosion notch on the flange of an I-beam

1.1. Weathering Steel

Since its first application in 1933 [**1**], weathering steel has been a primary construction material for bridges in the United States because of performance benefits, as well as for economic and environmental reasons. A large number of WS bridges has been built since 1964 [**2**]. Weathering steel is a high strength and low-alloyed structural steel. Weathering steel exhibits increased resistance to

atmospheric corrosion due to a protective layer on its surface under the influence of the weather. Florida Department of Transportation has initiated a program to identify locations for use of unpainted weathering steel for bridge structures because significant cost savings are anticipated versus carbon steels [**3**]. However, weathering steel does not form a protective layer if the following conditions are not met: 1. Atmospheric exposure to intermittent wet-dry cycles without prolonged wet periods; 2. Absence of heavy concentration of corrosive pollutants, especially deicing salts; 3. Washing of the exposed surface by rainwater; 4. Absence of detail geometrics that trap moisture, dirt, or debris and hence foster corrosion [**1**]. Due to these unmet conditions, corrosion notches are formed and observed as shown in Fig. 1 on the flange of steel I-beams where dirt and debris accumulate in aggressive environments [**4**]. These notches were seldom considered in previous studies and they may seriously jeopardize the structural safety of a bridge.

1.2. Atmospheric Corrosion Mechanism on Weathering Steel Structures

During raining period, wind driven rain water is directly accumulated on the flange of I-beams and/or obstructed by the web of I-beam structure and then flows down on the flange. Due to detail geometrics that trap moisture on some structures, rain water is accumulated on the flange which creates prolonged wet periods. Corrosion occurs on the area of accumulation of rain water and other foreign

substance. Rain water and deposited salt particles produce electrolyte containing chloride that causes severe corrosion on WS structures.

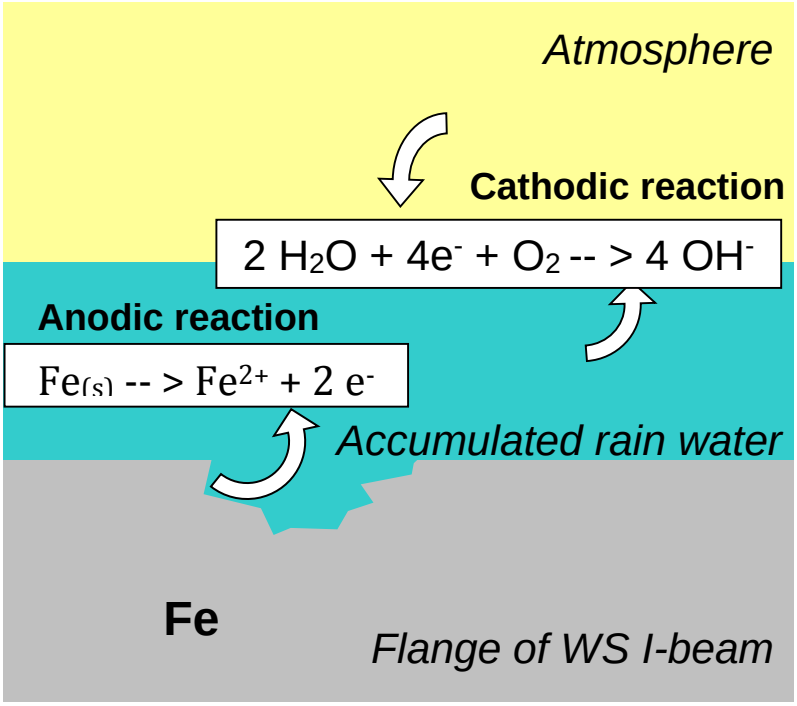

Figure 2 Atmospheric corrosion mechanism

In this process, it is atmospheric corrosion that takes place on steel structures. Like other types of corrosion, atmospheric corrosion involves an anode and a cathode. As shown in the diagram above, iron, which is the main composition of weathering steel, is both the anode and the cathode during this process. The part where the notch grows is the anode and the surrounding parts are the cathode. Accumulated rain water on the flange acts as the electrolyte, and the atmosphere provides oxygen that accelerates the corrosion process. The anode oxidizes with help of electrolyte or rain water and oxygen. Because this process usually takes a large amount of time before obvious corrosion can be observed, an accelerated method is presented in this thesis study.

2. BACKGROUND

2.1. Corrosion Rate

Corrosion processes are most often electrochemical. The dry-cell analogy is often used to describe this phenomenon [**5**]. The electrode at which chemical reduction occurs is called the cathode and the electrode at which chemical oxidation occurs is called the anode. Electron current is carried by the metal while ion current is carried by the ions in the requisite electrolyte. Weathering steel structures mostly corrode very slowly under atmospheric corrosion when exposed outside. Their corrosion tendency and rates largely depend on the components of the structure and the weather. However, in the laboratory, one can accelerate the corrosion process by increasing the corrosion rates.

The speed of a corrosion process is mainly a function of the reaction rates at the interface between an electrode and an electrolyte, i.e. corrosion rates. The corrosion rates are often described by the weight loss [**6**] or the corrosion current [**5**]:

$$R = \frac{KW}{ATD} \quad (1)$$

Where *R* is the corrosion rate, *K* is a constant, *T* is the time of exposure, *A* is the area of the specimen exposed, *W*, the weight loss and *D*, its density.

$$I_{corr} = \frac{I_{appl}}{2.3\Delta\phi}\left(\frac{\beta_c\beta_a}{\beta_c+\beta_a}\right) \quad (2)$$

Where β_c and β_a refer to Tafel constants for the cathodic and anodic reactions, and $\frac{I_{appl}}{\Delta\phi}$ is the polarization slope in the region near the corrosion potential.

There is also a very commonly used relation between the mass loss and the corrosion current, called Faraday's Law:

$$m = \frac{ITa}{nF} \quad (3)$$

Where *m* is the mass loss during the corrosion reaction, *I* is the corrosion current, *T* the time of exposure, *a* the atomic weight, *F* is Faraday's constant (96,500 Coulombs/equivalent) and *n* the number of equivalents exchanged. This relation is often used to calculate the mass loss of a corroding element by measuring the corrosion current.

2.2. Main Factors Affecting Corrosion Rate

2.2.1. External Current Source

As illustrated in Fig. 2, to accelerate the corrosion or oxidation process of the anode (Cu), an external current source is applied. The positive pole of this source is connected to the anode so that the electrode is polarized. Therefore, the anode has always the tendency to oxidize because it is not at equilibrium. Also according to Equation 2 and 3, the larger the applied current, the faster the anode oxidizes.

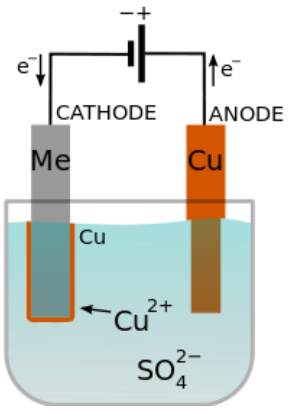

Figure 3 Electroplating of a metal with copper in a copper sulfate bath

In a study of fatigue crack initiation from corroded hemispherical notches in aerospace structural materials [**7**], Garcia et al. have applied a 1.5 V direct current provided by a Buehler ElectroMet-Etcher to accelerate the corrosion process of notches on aluminum specimens.

2.2.2. Electrolyte

As carrier of the current, the ions in the electrolyte play an important role in corrosion rate. The more ions exist, the easier the current goes through. Garcia et al. have used a mixture of de-ionized water, nitric acid and NaCl as the electrolyte in the corrosion cell [**7**]. Also, studies [**5**] show that the corrosion rates increase as the quantity of dissolved oxygen in the electrolyte increases.

2.2.3. Passivation

A metal is passive if, on increasing the electrode potential toward more noble values, the rate of anodic dissolution in a given environment under steady-state conditions becomes less than the rate at some less noble potential [**8**]. An

example of iron made anode in 1N H_2SO_4 is given in Fig. 4 below [**5**]. Iron becomes passive at a higher potential, and the corrosion rate drops.

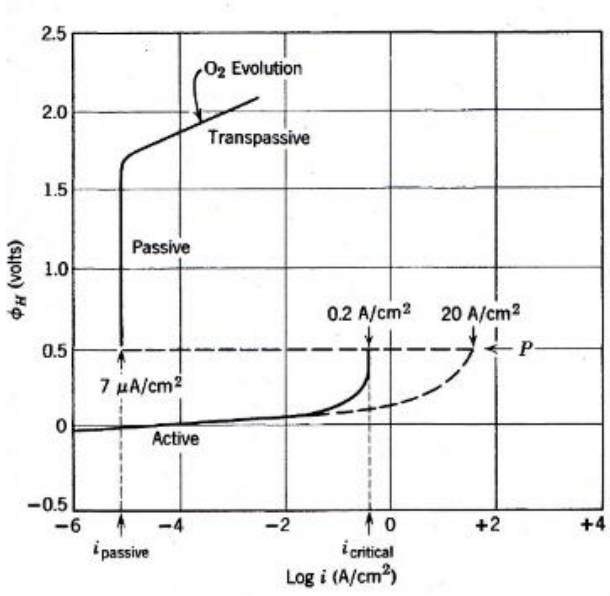

Figure 4 Potentiostatic anodic polarization curve for iron in 1N H_2SO_4

Alternatively, a metal can become passive on increasing concentration of an oxidizing agent. Therefore, to guarantee a high rate of corrosion, excessive potential or/and concentration of electrolyte should not be applied.

2.3. Electrochemical Machining

In industrial microsystem technologies, electrochemical machining (ECM) is used for precise shaping on hard metals. To guarantee a high metal removal rate, a large current (up to 70 A/cm^3) and a high flow rate of electrolyte are often applied (up to 7 m/s) [**13**]. This method is efficient, a similar method is applied in this thesis study and presented in the next chapter.

2.4. Scanning Electron Microscope (SEM)

The SEM in the Materials Lab at Seatech was used to observe the fracture surface of WS samples after tensile tests (fractography). The large depth of focus, the possibility of changing magnification over a large range and simple sample preparation make the SEM ideal for the observation in this thesis study.

2.5. Corrosion Fatigue of Weathering Steel

2.5.1. S - N Diagram

In high-cycle fatigue situations, the results of fatigue tests are presented in S-N (S represents the stress range and N the Number of cycles to failure) plots of stress range versus the base-10 logarithm of numbers of cycles to failure, N. An example is provided in Fig. 5.

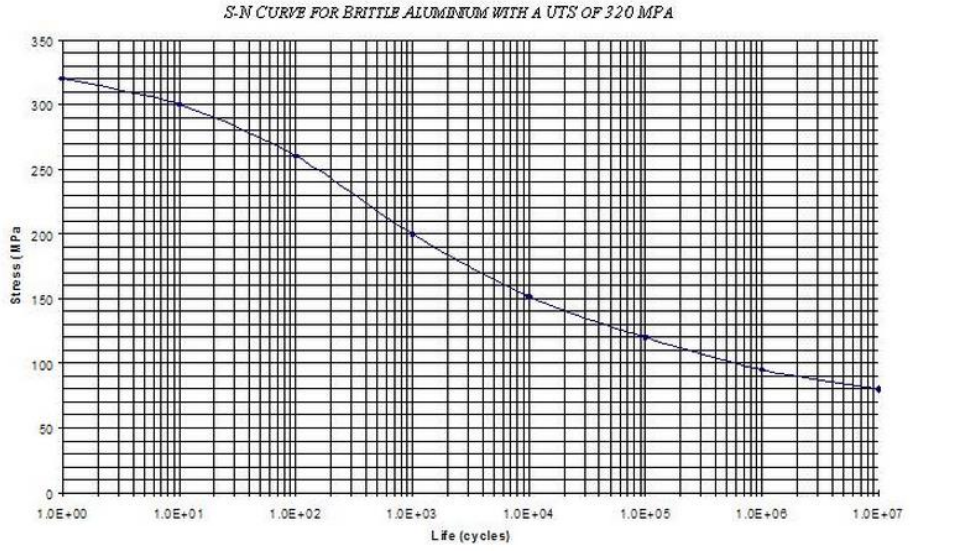

Figure 5 S-N curve for brittle aluminum with a UTS (Ultimate Tensile Strength) of 320 MPa

2.5.2. Fatigue Notch Factor due to Corrosion

Albrecht et al. [**9**] identified three significant factors which contribute to the total reduction in fatigue strength of a corroded beam member such as corrosion factor, environmental factor and pitting factor. To simplify the process, Albrecht et al. combined all three factors in to one fatigue notch factor. The fatigue notch factor is defined at certain number of cycles (often 500,000 cycles) as the ratio of the mean stress range for AASHTO (American Association of State Highway and Transportation Officials) Category A (fatigue strength decreases from category A to E) rolled beams, f_{rA} (solid circle), and the mean stress range of the detail under consideration, f_{r1} (open circle) due to corrosion [**1**].

$$K_f = \frac{f_{rA}}{f_{r1}} \qquad (4)$$

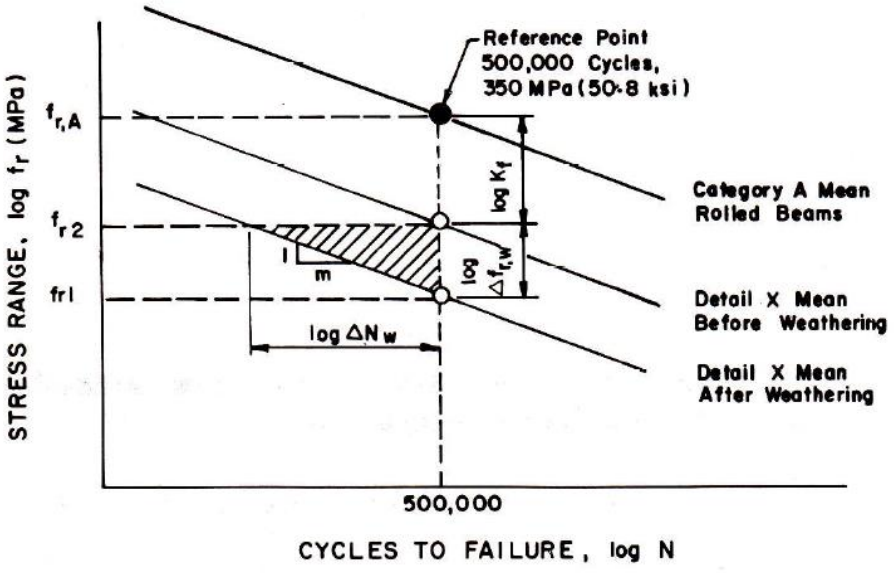

Figure 6 Definition of fatigue notch factor

The fatigue notch factor allows us to quantify the loss in stress range due to corrosion.

2.5.3. Previous Studies on Fatigue Behavior of Weathering Steel

As presented in the introduction (section 1.1), the effects of corrosion notches are often neglected in previous studies. Most of these studies have been made on the A588 weathering steel and have been done after a long period of continuous weathering (up to 11 years) [**1**]. However, no study has focused on the effect of corrosion notches. To shorten the weathering time, Albrecht [**10**] tried to artificially weather A588 specimens in laboratory by subjecting them to 1800 wet-dry cycles of 1-hour duration. However, a scanning electron microscope (SEM) revealed that the oxide coating was much more porous, coarse and poorly bonded to the steel base than the coating grown naturally outdoors. A review of the methods and results from previous studies are briefly presented below:

- Between 1972 and 1983, 8 different types of weathering steel specimens have been subjected to fatigue tensile test [**1**]. Most of them were welded or stiffened. Conclusion from these studies was that the weathering reduced dramatically the fatigue life. This reduction varied from 40 to 70% of original fatigue life, depending on the weathering period and the stress range.
- More recently, in 1994 and 2009, Albrecht et al. [**11**][**12**] have conducted two studies about the fatigue strength of weathered A588 steel beams.

These two studies are similar except that rolled-beam specimens are used in 1994 and welded and cover-plated beam specimens are used in 2009. During the study in 2009, one set of beams was boldly exposed to the environment; the other was exposed under a metal deck that simulated the shelter provided by highway bridge decks and was slightly sprayed with a salt solution during winter months. All beams were 4724-mm and were tested on a 4572-mm span. Two beams were simultaneously tested in a dual-beam test frame. Each beam was loaded with one actuator (either 220 or 90 kN). A spreader beam distributed the load to two points spaced 914 mm apart. The wave form of the loading cycle was sinusoidal and of constant amplitude. The loading frequency was 0.75 Hz. A beam was said to have failed when at least 50% of the tension flange cracked. The fatigue notch factor (Equation 4) and the AASHTO fatigue design specifications were used to quantify the loss in fatigue stress range. Results showed that the degradation of sheltered beams was more severe. And the author suggested that severely degraded weathering steel members should be painted without delay.

- A study about the crack initiation from corroded hemispherical notches is briefly mentioned in the section 2.2 of this chapter. Even though the study is not about weathering steel, its fatigue test method is interesting [**7**]. The dog-bone specimens are made from aluminum 7075-T7351 and D6AC steel. After the notch and corrosion process, the specimens are measured

and instrumented for direct current potential drop (PD) for the Fracture Technology Associates (FTA) test and data acquisition system. The PD method detects the crack propagation from the notch through the change in electric potential due to change in cross-sectional area of the crack. A step testing is applied and the starting load ratio is R = 0.1 or 0.7 until a crack of 0.25 mm is detected or 3×10^6 cycles is reached. If 3×10^6 cycles is reached before cracking, the load is then increased by 10% and the test is started all over again. This step testing is used to determine a threshold load or endurance limit depending on the critical parameter.

3. PHASE 1 – NOTCH CREATION METHODS AND RESULTS

Studies related to corrosion usually take years or more because most of the atmospheric corrosion processes are very slow. Due to time constraint of Master's thesis study, principles of electrochemistry are applied to increase the corrosion rate on weathering steel samples.

3.1. Weathering Steel Samples

The weathering steel samples in this thesis study are A606 - 04 Type 4 cold-rolled plates. Their tensile requirements and chemical composition are shown in Table 1 & 2 respectively.

Table 1 Tensile specifications of A606-04 Type 4 cold rolled weathering steel material

Tensile strength MPa (ksi)	468 (68)
Yield strength MPa (ksi)	408 (59.2)
Elongation in 50 mm, %	32

Table 2 Chemical composition for A606-04 Type 4 cold rolled weathering steel material

Chemical Element	Composition, %
C	.05
Mn	.86
P	.008
S	.001
Si	.37
Cu	.29
Ni	.28
Cr	.56
Mo	.01
Sn	.009
Al	.04
V	.053
Nb	.001
N	.008
Ti	.005
B	.000
Ca	.002
Sb	.002

3.2. Notch Creation Methods

The samples in this thesis study were plates made of weathering steel described in section 3.1. Their dimensions were 101 x 76 x 1.62 mm as shown in the SolidWorks plan below. All the samples were cleaned by sand blasting. This process eliminated the existing corrosion products. Then the samples were dipped in methanol, drained on clean laboratory paper and dried with hot air for 2 minutes to prevent water condensation. Then all the samples were labeled by permanent marker. The objective of this first phase was to create notches of appropriate breadth in the middle of the each plate's surface in a short amount of time by corrosion. These plates with notches were cut into smaller pieces in order to perform static and fatigue tests on them in the second phase of this study.

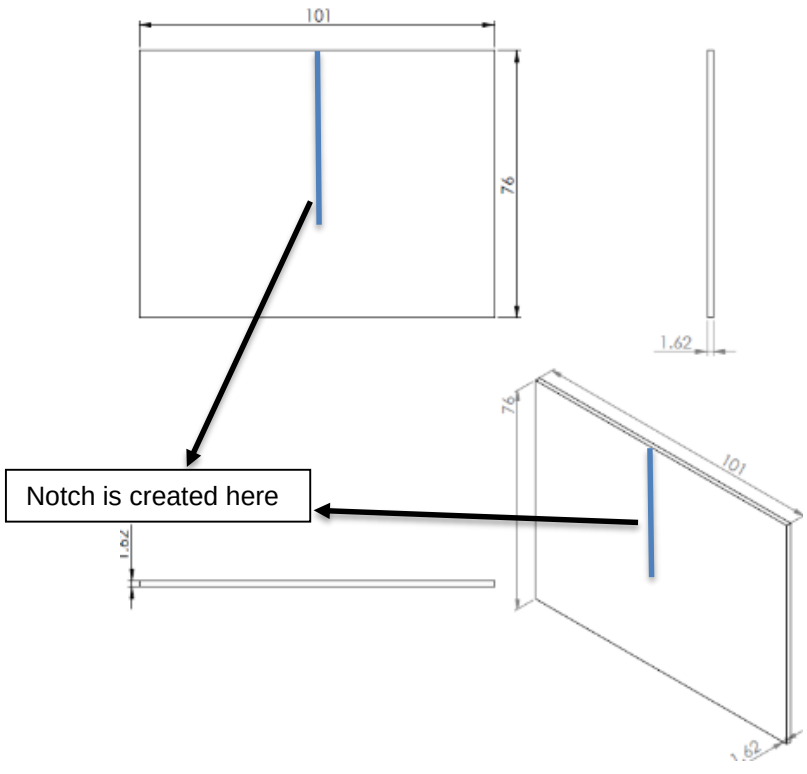

Figure 7 Sample dimensions and notch location

Based on the previous reviews [**7**][**13**], a large current should be applied in an electrochemical circuit through an electrolyte of appropriate concentration of sodium chloride in order to significantly increase the corrosion rate on the surface of weathering steel plates without passivating them.

Also two conditions on the geometry of the notches must be satisfied:

1. The sample must be under plane stress condition during the fatigue test in the second phase, which means the breadth of the notch or the plastic zone size should be close to the thickness of the sample. This is usually the case with the corrosion notch observed on the flange of WS I-beams. In this study, a notch size of 3 mm is applied;
2. Because the original thickness is very small (approximately 1.62 mm), the remaining thickness in the notch should not be too small so that the samples won't fail too quickly during the fatigue tests. Remaining thickness is from 1.1 to 1.3 mm for the WS plates in this study, which means the notch depth varies from 0.3 to 0.6 mm. The remaining thickness or the notch depth varies also in each sample.

Two attempts/methods were carried out in this study.

3.2.1. First Attempt on Notch Creation

Because there weren't similar studies to this thesis study to refer to, parameters such as the current density and configuration of the system were hard to determine in the beginning.

For the first attempt, which was proposed in this thesis proposal, a current of 125 µA was applied and the configuration can be seen from the diagram below.

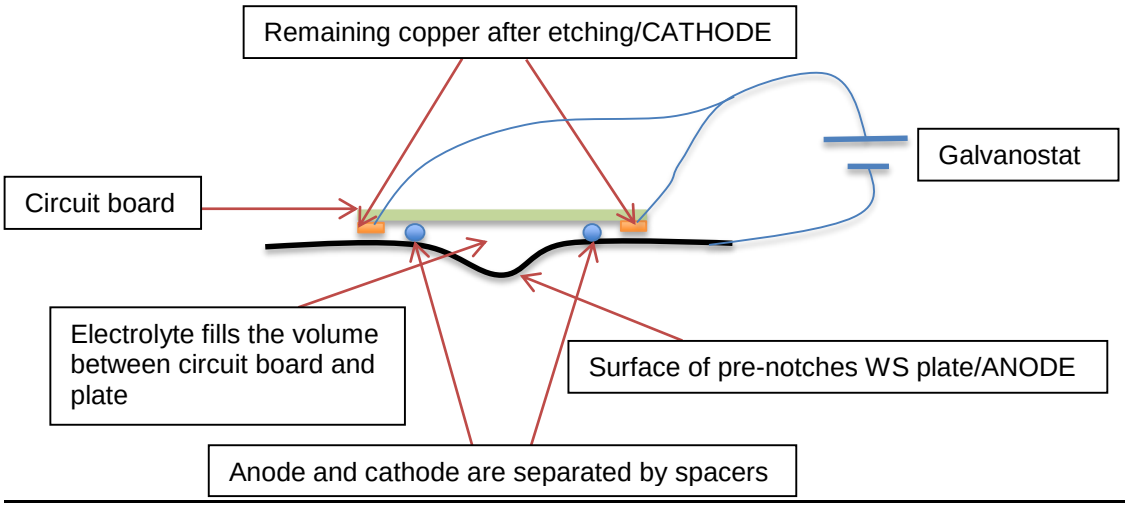

Figure 8 Circuit configuration for the first attempt

As proposed in the thesis proposal, 4 tasks were carried out for this attempt:

1. The samples were pre-notched mechanically by using a mill drill in the middle across the surface and perpendicular to the edge. The pre-notched area would be the anode.
2. The anode was prepared in this task. The notch of the WS plate was the anode and the circuit boards with copper coating (Fig. 9) was the cathode. First the circuit board needed to be cut into small pieces as shown in Fig. 10 to be able to cover the pre-created notch. Also shown in Fig. 10, the small piece was covered by straight decal patterns on the sides and is put in an etching solution (ferric chloride) to dissolve the copper in the middle. Each small piece of circuit board had two functions: 1. To reduce the oxygen concentration in the notch so that the notch will become an anode;

2. The two remaining strips of copper on the circuit board served as the cathode.

Figure 9 Circuit board and straight decal patterns

Figure 10 Small piece of circuit board with decal patterns on in etching solution

3. Both the anode and the cathode were prepared. The electrochemical circuit needed to be configured as shown in Fig. 8 above. This configuration was realized as shown in the photo (Fig. 11) below. The electrolyte came from a nozzle on top, which was supplied by a reservoir positioned at a higher location. Direct contact between the anode (WS plate at bottom) and the cathode (copper piece on top) must be avoided to prevent a short circuit. They were electrically separated by spacers but in contact with the electrolyte. Certain area of the WS plate was taped so

that the corrosion would be concentrated on the pre-notched area. A current of 125 μA provided by a galvanostat flowed through the circuit. This galvalnostat consisted of a battery and a rheostat.

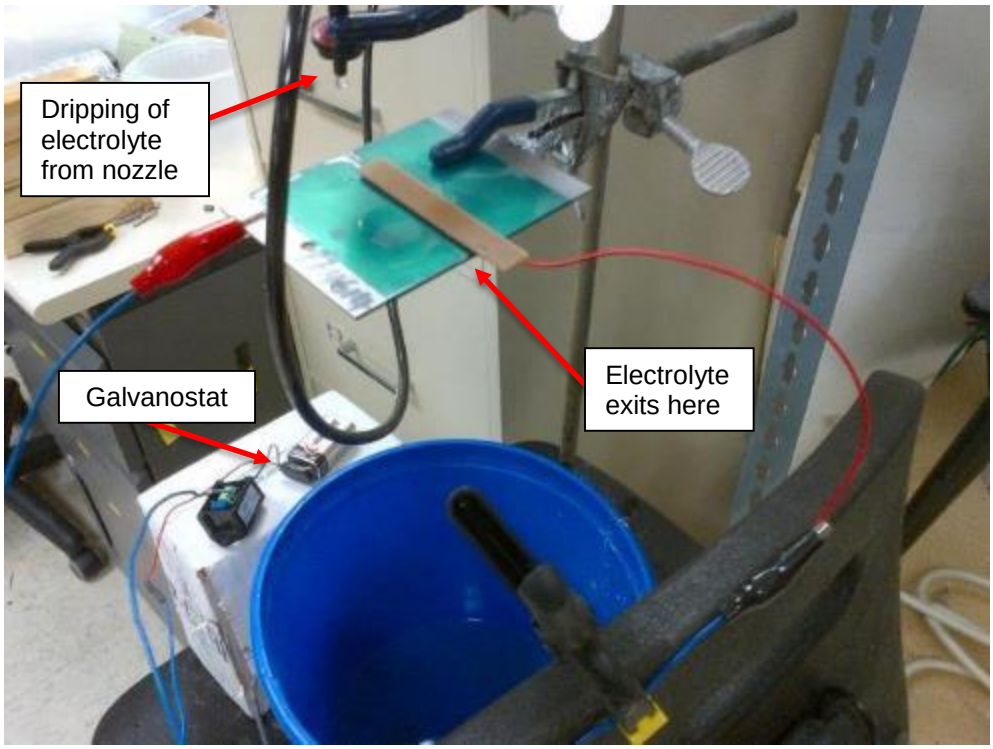

Figure 11 Notching setup and circuit configuration

4. The constant current of 125 μA was applied until observation of notch of desired size.

3.2.2. Second Attempt on Notch Creation

To improve the notch creating process, a much larger amount of current and electrolyte were applied in this attempt. For each plate sample, a current of 4 A was applied for a period of 10 minutes. Experiments showed that this amount of current and time could create notches that satisfied the two conditions above.

The current was provided by an Epsco D-612T power supply in the Material Lab. According to Equation (3) the Faraday's Law, a total amount of removed weathering steel can be calculated depending on the form of the rust:

If only Fe^{2+} ions (ferrous ions) are formed after the corrosion:

$$m = \frac{ITa}{nF} = \frac{4 \times 10 \times 60 \times 55.845}{2 \times 96485} = 0.69\ g \quad (5)$$

If only Fe^{3+} ions (ferric ions) are formed after the corrosion:

$$m = \frac{ITa}{nF} = \frac{4 \times 10 \times 60 \times 55.845}{3 \times 96485} = 0.46\ g \quad (6)$$

With *a* = 55.845 g/mol is the atomic weight of iron.

Therefore, depending on the corrosion product, the total amount of removed steel on each plate should be between 0.46 g and 0.69 g by ignoring other metals in the steel.

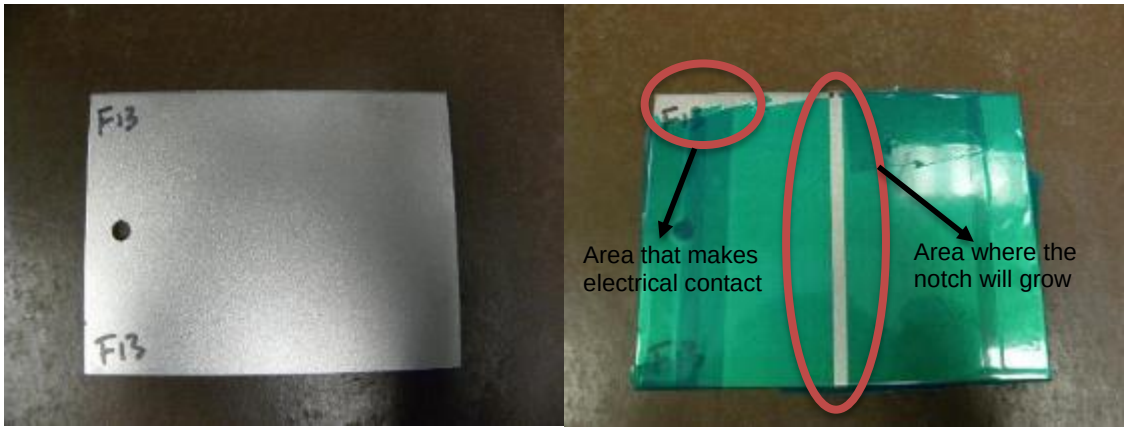

Figure 12 Taping on the sample plate

2 molar sodium chloride was chosen to be the electrolyte, which was 117 g of sodium chloride in 1000 ml of water. This concentration of sodium chloride was enough to let current flow and did not cause any passivation on the plate samples.

While the WS plate samples were the anode, a copper bar was used as the cathode, which was a more noble metal than iron.

A preparation process was followed for each plate before the notch creation to guarantee the consistency of experiments:

1. The plates were entirely covered by waterproof tape except the area that made electrical contact and the area where the notch was going to be formed. Fig. 12 shows an example of this configuration;

2. Both the WS plate and the copper bar were partially slotted in a piece of polymer as shown in Fig. 13 below before immersed in the electrolyte of sodium chloride in a cylinder container. Three screws were positioned around the inner circumference of the cylinder container that would be covered by the polymer piece. Both the polymer piece and screws prohibited any movement of anode and cathode with respect to each other and with respect to the container. This fixation of anode and cathode provided notch shape uniformity on every sample.

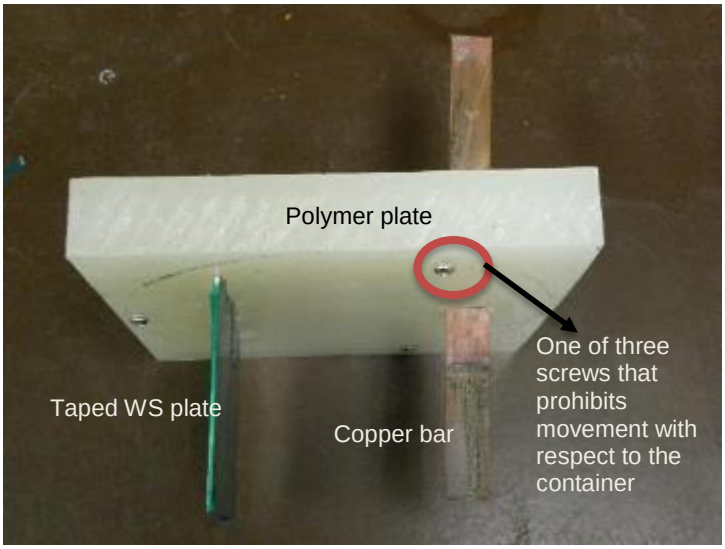

Figure 13 Taped WS sample and copper bar slotted in polymer plate

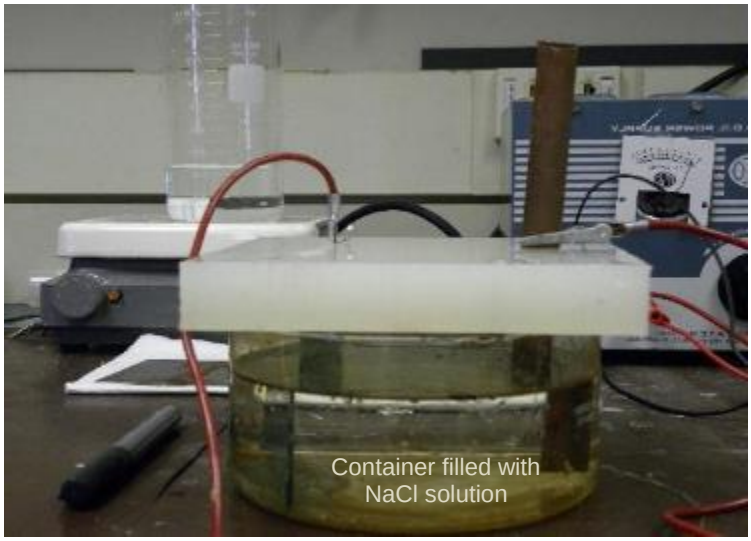

Figure 14 WS plate and copper bar immersed in electrolyte with electrical connections

3. The electrolyte was prepared by 2 moles of sodium chloride solution, which was 117 g of sodium chloride in 1000 ml of water.
4. Preparation of the electrical circuit: a current of 4 A was provided by the Epsco D-612T power supply. Two multimeters were used to monitor the current through the electrolyte and the voltage between the anode and the cathode.

The anode/WS plate was connected to the positive pole of the power supplier and the cathode/copper bar was connected to the negative pole. Diagram and photo below show the circuit.

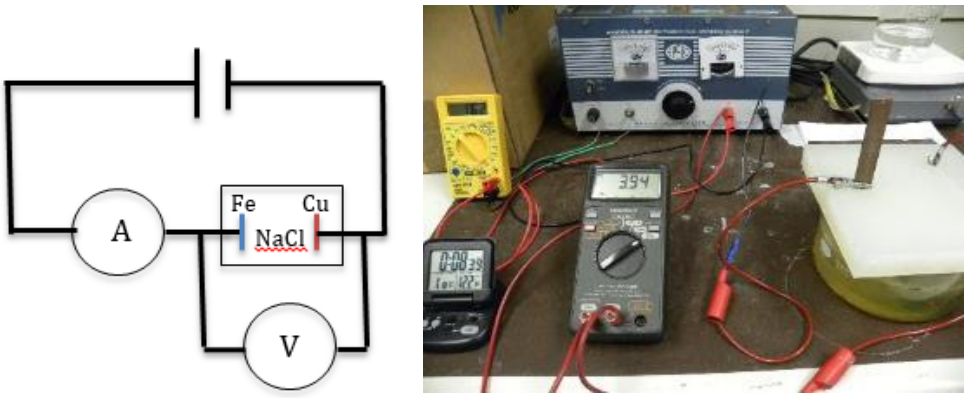

Figure 15 Circuit configuration for second attempt and its realization

Reactions on cathode/copper bar:

$2H^+ + 2e^- \rightarrow H_2$ (main reaction) and;

$2H_2O + 4e^- + O_2 \rightarrow 4OH^-$.

Reactions on anode/WS plate:

$Fe \rightarrow Fe^{2+} + 2e^-$;

Reactions in electrolyte:

$Fe^{2+} + 2OH^- \rightarrow Fe(OH)_2$;

$4Fe(OH)_2 + O_2 + 2H_2O \rightarrow 4Fe(OH)_3$;

$\rightarrow 2Fe_2O_3.H_2O + 4H_2O$ (RUST).

5. The current monitored by the multimeter was controlled to be around 4 A. The voltage between the anode and the cathode varied from 16 V to 17 V.

3.3. Results of Phase 1

3.3.1. Results from First Attempt

The first attempt wasn't successful because the corrosion process was very slow. Some uniform corrosion can be observed, but no obvious notch formation was observed after 6 days of constant supply of current and electrolyte (see Fig. 16 below). In addition, there was no obvious weight loss of WS plate samples.

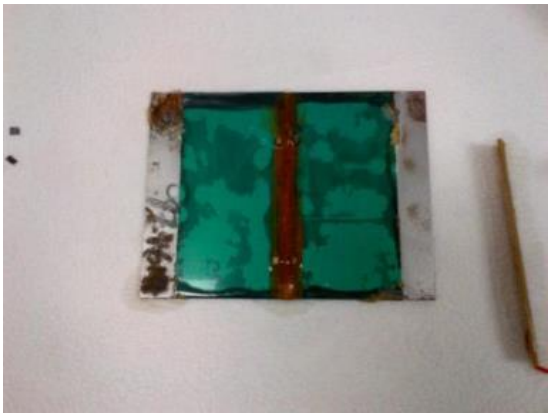

Figure 16 Result from attempt

Two reasons have caused this failure:

1. The current was very small;
2. The flow rate of the electrolyte was small, so that the corrosion product would not be flushed out. Also, passivation may have occurred on the surface of the pre-notched area of WS plate.

However, a larger current with a larger electrolyte flow rate would induce more significant corrosion on samples.

3.3.2. Results from Second Attempt

Improved from the first attempt, the second attempt turned out to be satisfactory.

3.3.2.1. Weight Loss

The weight loss of WS plate samples is the most straightforward way to describe the corrosion effect. There are 27 plates that have been corroded in total. Their weight losses are shown in the Table 3 on the next page. As mentioned before, all these plates were subjected to similar conditions of corrosion, including corrosion current, corrosion time and position of anode and cathode.

Designations “S” and “F” represent samples that would be subjected to static test and fatigue test respectively in the second phase. The average weight loss of WS plate samples was approximately 0.5 g. The minimum weight loss was 0.4677, which was greater than that predicted for only ferrous ion formation and the maximum weight loss was 0.5509, which was less than that predicted for only ferric ion formation. This implied that both Fe^{2+} and Fe^{3+} were generated from every sample during the corrosion process. Also a small standard deviation of 0.018 proved the consistency of corrosion processes.

Table 3 Weight losses of WS samples caused by corrosion

Sample N'	Original Weight (g)	Weight after corrosion (g)	Weight Loss (g)
S3	98.3846	97.8564	0.5282
S4	94.4987	94.005	0.4937
S5	98.0559	97.5614	0.4945
S6	98.4175	97.926	0.4915
S7	97.5361	97.0013	0.5348
S8	97.6946	97.2017	0.4929
S9	97.161	96.6635	0.4975
F1	97.8049	97.3111	0.4938
F2	98.419	97.9085	0.5105
F3	98.6452	98.0943	Max: 0.5509
F4	96.6783	96.1716	0.5067
F5	98.4275	97.9486	0.4789
F6	94.9899	94.5003	0.4896
F7	96.7552	96.2513	0.5039
F8	94.5662	94.0739	0.4923
F11	97.7849	97.2555	0.5294
F12	96.9617	96.4785	0.4832
F13	98.2363	97.7686	Min: 0.4677
F14	96.5682	96.0815	0.4867
F15	94.4194	93.9162	0.5032
F16	97.1543	96.6506	0.5037
F17	96.1959	95.6709	0.525
F18	97.5099	97.0056	0.5043
F19	96.2701	95.7586	0.5115
F20	98.7866	98.2691	0.5175
F21	98.2371	97.7274	0.5097
F22	98.4369	97.9336	0.5033
		Average:	0.50385
		Standard deviation	0.018042

3.3.2.2. Shapes and Dimensions of the Notches

Even though the corrosion/anode dissolution processes were consistent for WS plate samples, the shapes and depths of the notches varied slightly from each other. The breadth of the notch was controlled to be 3 mm by taping as shown

before. However, depending on the sealing condition of the tape, electrolyte could enter in between the tape and the sample, which caused larger breath at certain locations. This is shown below by comparing two notches below. Notch 1 has very straight edges while notch 2 is in an irregular shape. Trace of electrolyte can be seen on two sides of notch 2.

The cross section of the notch is also illustrated in Fig. 17 below.

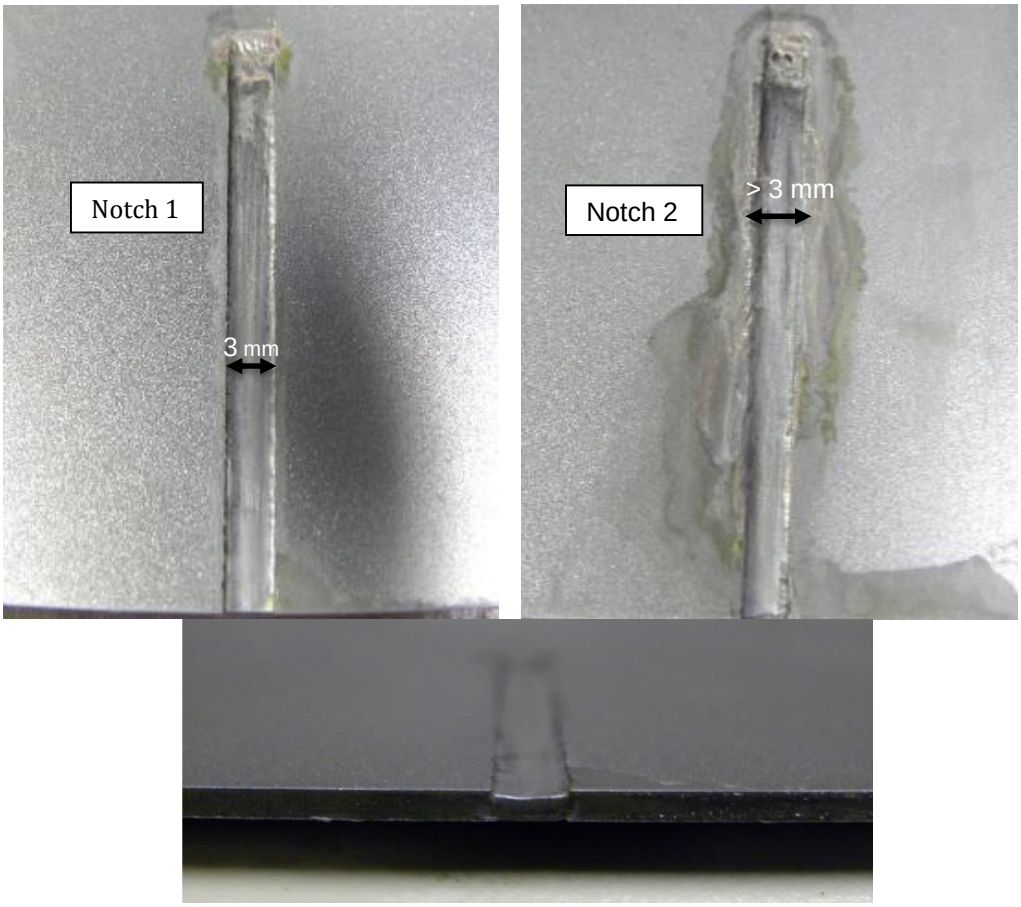

Figure 17 Shape of the notch created by corrosion

Remaining thickness was from 1.1 to 1.3 mm for the WS plates in this study, which meant that the notch depth varied from 0.3 to 0.6 mm. This depth varied not only from sample to sample but also varied along the notch. This variation

caused by corrosion led to variation in cross section area, which played an important role in fatigue testing.

To accurately shape the notches and to keep records, all the notches were molded by epoxy putty to illustrate their volumes as shown below. They were labeled with a permanent marker.

Figure 18 Molds for WS samples

The depths of the notches or the remaining thicknesses of the samples were deduced from these molds. As shown in Fig. 19, the photo of the mold of sample F7, a bump can be seen in the middle. This is the mold of the notch. Therefore, the thickness of this bump is the corresponding notch's depth. This is obtained by the difference of the thickness of the mold at the top of the bump (location A) and the thickness at the flat surface around (location B). These two thicknesses were measured by a digital caliper.

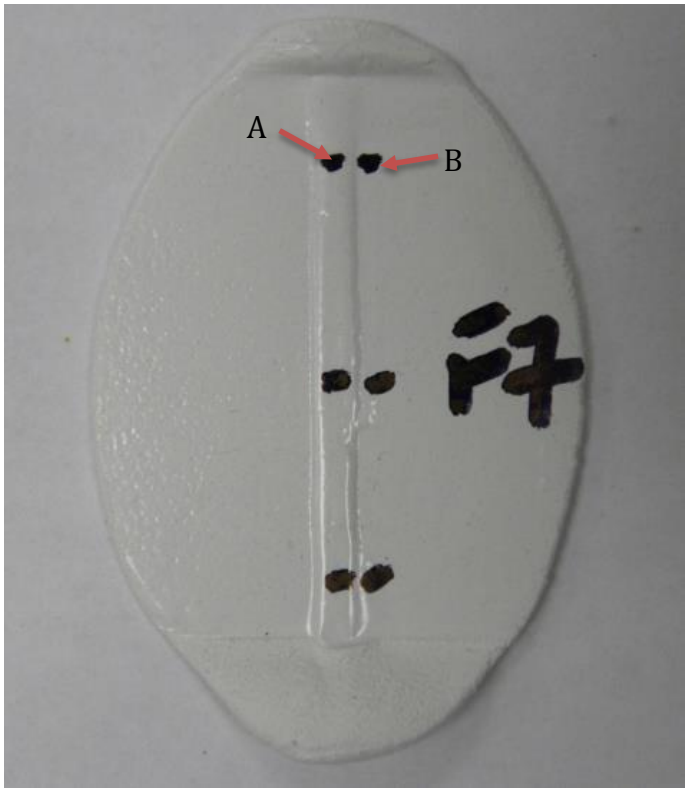

Figure 19 Mold for sample F7

For every sample's mold, three differences were calculated for a mean value. And the remaining thickness was calculated by a subtraction from 1.62 mm, which was the original thickness of samples. These measurements and calculation were listed in Table 4 below.

The results in the last column of above table were used to calculate the remaining cross section area in the notches in Phase 2.

Table 4 Notch depths and remaining thickness for WS samples

Sample N'	Thickness at location A (mm)	Thickness at location B (mm)	Notch depth (mm)	Mean Value (mm)	Remaining Thickness (mm)
F1	3.8	3.34	0.46	0.38	1.24
	3.55	3.2	0.35		
	3.34	3.02	0.32		
F2	2.25	1.82	0.43	0.44	1.18
	2.37	1.96	0.41		
	2.49	2.01	0.48		
F3	2.73	2.13	0.6	0.50	1.12
	2.75	2.26	0.49		
	2.82	2.4	0.42		
F5	2.88	2.42	0.46	0.42	1.20
	2.86	2.44	0.42		
	2.82	2.43	0.39		
F6	2.99	2.52	0.47	0.48	1.14
	2.3	1.85	0.45		
	1.8	1.27	0.53		
F7	2.17	1.8	0.37	0.36	1.26
	2.2	1.85	0.35		
	2.26	1.9	0.36		
F12	2.09	1.56	0.53	0.52	1.10
	2.15	1.6	0.55		
	2.19	1.7	0.49		
F13	2.75	2.32	0.43	0.39	1.23
	2.45	2.07	0.38		
	2.1	1.73	0.37		
F14	2.42	1.92	0.5	0.43	1.19
	2.47	2.03	0.44		
	2.5	2.14	0.36		
F15	2.64	2.1	0.54	0.47	1.15
	2.49	2.05	0.44		
	2.35	1.93	0.42		
F17	2.12	1.62	0.5	0.44	1.18
	2.35	2.03	0.32		
	2.61	2.1	0.51		
F18	2.14	1.76	0.38	0.40	1.22
	2.42	2.06	0.36		
	2.68	2.23	0.45		
F19	2.46	1.98	0.48	0.46	1.16
	2.47	1.97	0.5		
	2.37	1.98	0.39		
F20	2.11	1.64	0.47	0.45	1.17
	2.21	1.77	0.44		
	2.31	1.86	0.45		
F21	2.55	2.16	0.39	0.41	1.21
	2.23	1.79	0.44		
	1.88	1.49	0.39		
F22	2.26	1.93	0.33	0.34	1.28
	2.47	2.13	0.34		
	2.66	2.3	0.36		

4. PHASE 2 – STATIC AND FATIGUE TESTS ON CORROSION NOTCHED WEATHERING STEEL SAMPLES AND RESULTS

To determine the loading level for the fatigue tests, at least three static tests should be done. All the static and fatigue tests were performed in tension.

4.1. Weathering Steel Samples

Corrosion notched WS samples from Phase 1 were tested in this phase. Before any of the static or fatigue tests, samples were approximately cut in half by water jet cutting machine. The advantage of water jet cutting is that it won't cause any stress concentration in the samples. The remaining width of the plate with notch was about 39 mm. The cutting by the water jet machine wasn't perfectly straight, a slope could be observed on the side that had been cut compared to another side. This would cause a slight difference in the cross section along the direction of testing force.

To make each test consistent with each other, whether it was a static test or fatigue test, the same gripped length should be guaranteed. Therefore, a gripped length of 1.5 mm was applied on both ends every time.

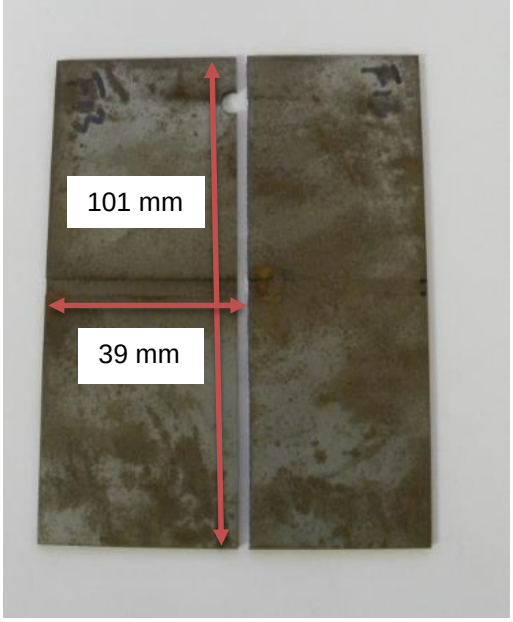

Figure 20 Plate sample cut to 39 x 101 mm

4.2. Static Testing Method and Results

Seven static tests were performed in total. However, only 3 data points were acquired. This was because a preset interlock stopped the crosshead of the MTS testing machine in the Material Lab at Seatech from moving further than 12 mm. This caused the machine to stop before the break of 4 other samples. Therefore, these 4 data points could not be considered.

4.2.1. Ultimate Loads

Data acquisition rate was 10 Hz and the operating speed was 2 mm/min. Since the cross section area was hard to quantify because of the irregularity resulting from notch formation, ultimate load was used instead of ultimate strength. The original ultimate strength before notching can be calculated as: 468 MPa X 1.62

mm X 39 mm = 29.57 kN. The ultimate loads are shown in the table below. The last column shows the loss in ultimate strength in percentage.

Table 5 Ultimate loads from static tests

Sample N'	Ultimate Load (kN)	Loss in Ultimate Strength
S4	19.933	32.59%
S7	21.559	27.09%
S9	25.323	14.36%
Mean Ultimate Load, P_{ult} (kN) :	22.272	24.68%

4.2.2. Elongations and Strains

The three samples in static test, S4, S7 and S9, were put together and photographed to illustrate their elongation compared to the other parts of the plate with original lengths of the samples. Then strains were calculated.

Figure 21 Sample S4

Figure 22 Sample S7

Figure 23 Sample S9

Some observations are made from above pictures:

1. Every sample has been elongated by around 2.5 mm;
2. Every sample has been narrowed in the middle (necking), where the notch has been. This proves that extensive plastic deformation has happened before fracture;
3. Ductile fractures can be observed from the fracture surface, a picture of which can be seen below. This phenomenon of ductile fracture has also been confirmed by SEM observation.

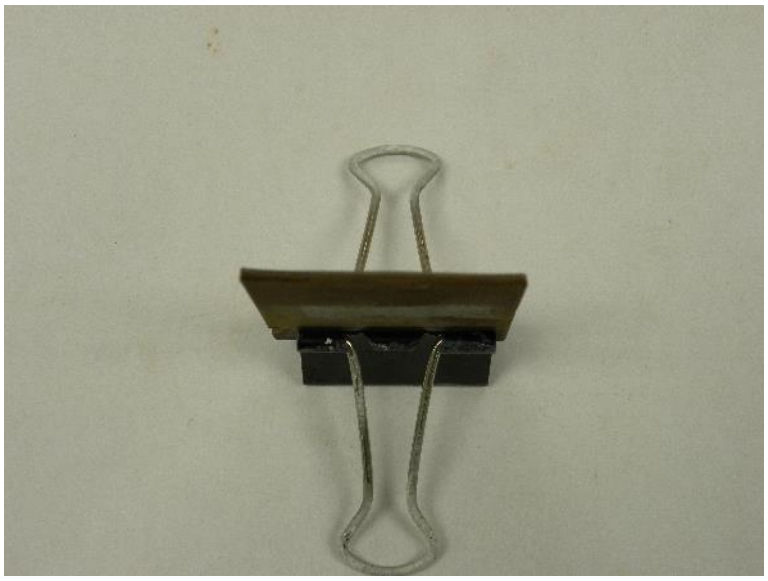

Figure 24 Fracture surface from static tests

Strains of the whole length of samples are calculated in the following table:

Table 6 Elongations and strains of static testing samples

Sample N'	Length after Fracture (mm)	Original Length (mm)	Elong. (mm)	Strain (%)
S4	103.69	101	2.69	2.66
S7	103.34	101	2.34	2.32
S9	103.98	101	2.98	2.95

It's also interesting to show the strains of the notches:

Table 7 Elongations and strains of static testing samples' notches

Sample N'	Width after Fracture (mm)	Original Width (mm)	Elong. (mm)	Strain (%)
S4	4	3	1	33
S7	4	3	1	33
S9	4.5	3	1.5	50

Interesting results can be seen from above. While the strain of the whole sample is around 2.6%, the strain of the notch can go up to 50%. Therefore, the corrosion made notches encountered severe deformation from tension.

In addition, the load-extension diagrams were plotted:

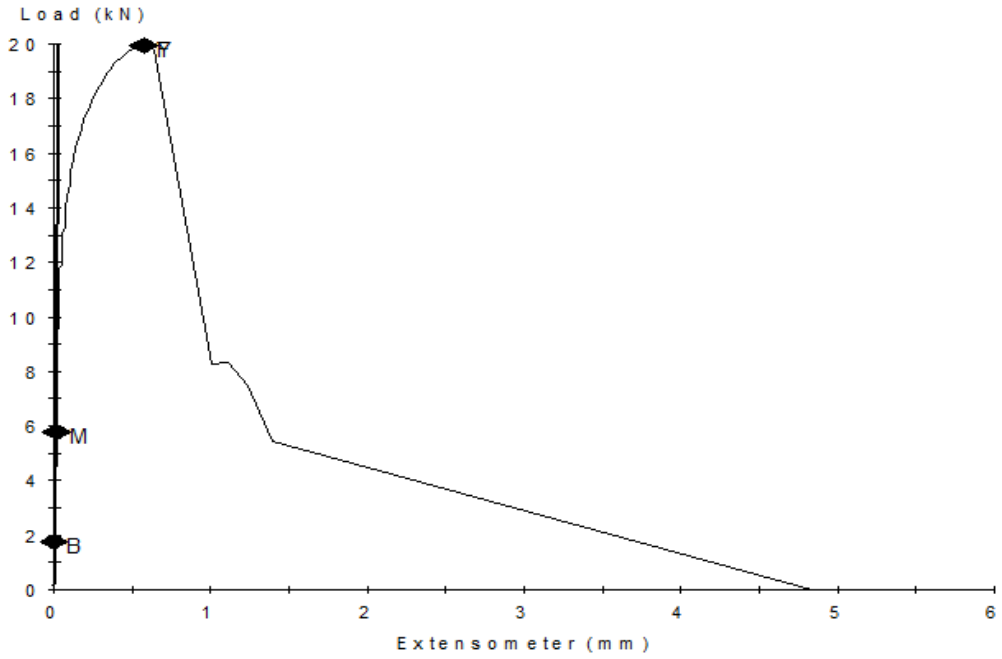

Figure 25 Load-Displacement diagram for sample S4

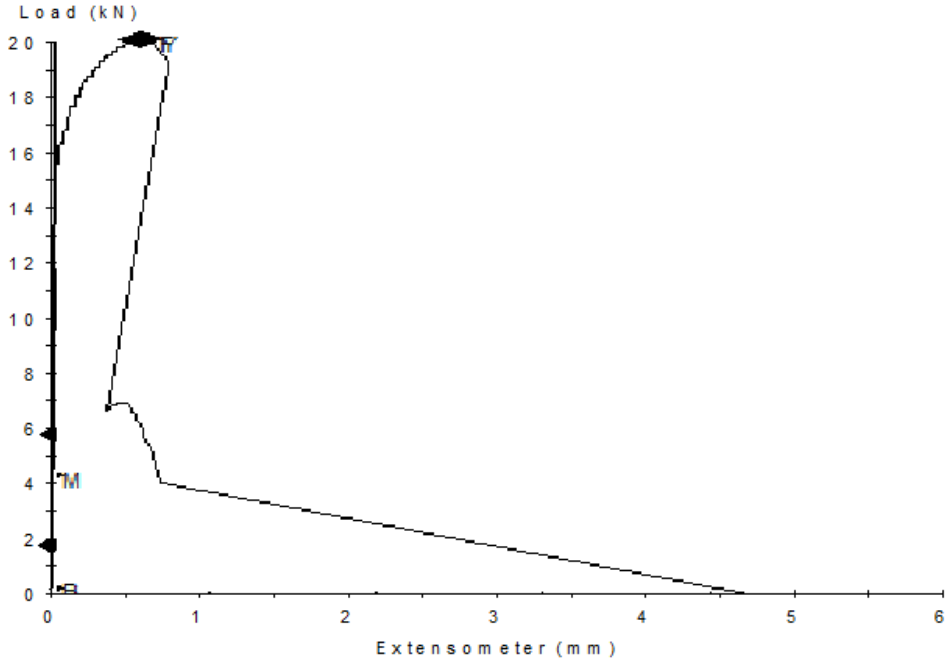

Figure 26 Load-Displacement diagram for sample S7

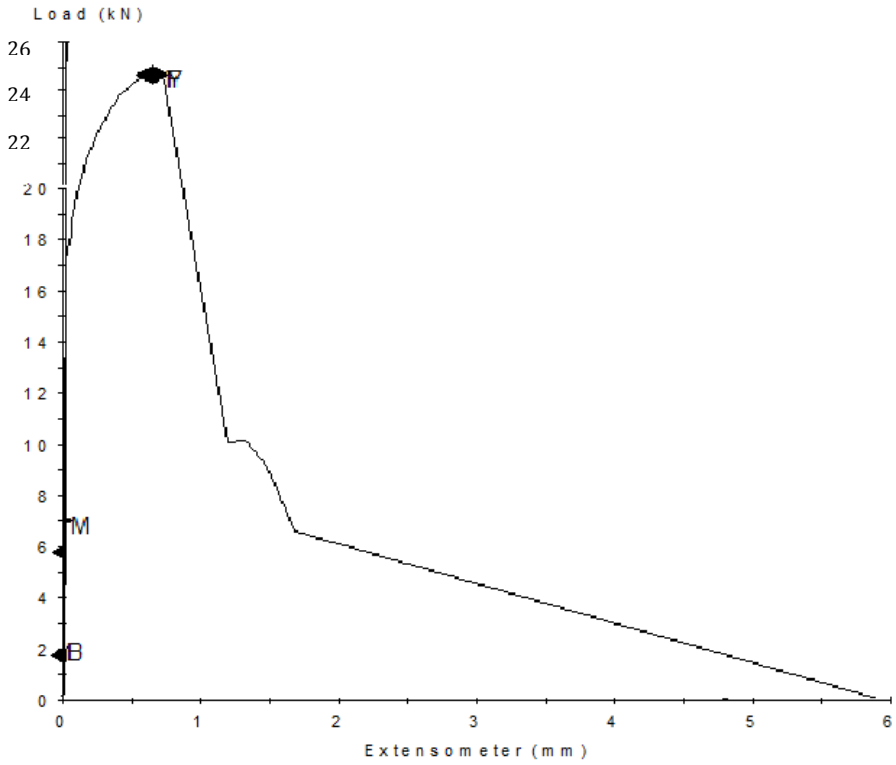

Figure 27 Load-Displacement diagram for sample S9

4.2.3. Microscopic observations of fracture surfaces by SEM (Scanning Electron Microscope)

The samples were cut in to 5 mm high with their original length of 39 mm to be able to fit into the observation chamber of SEM. This procedure was also followed before the observation on the samples after fatigue testing.

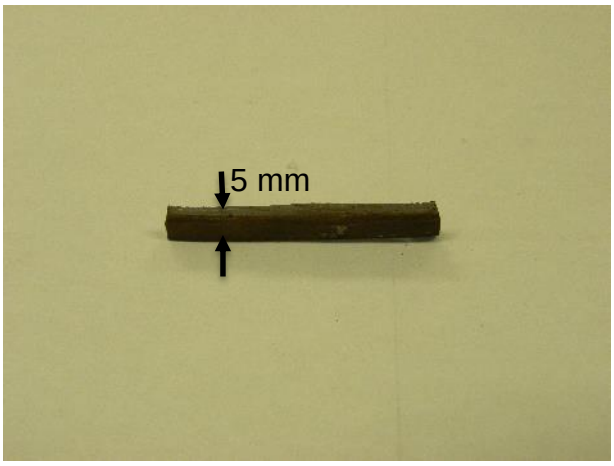

Figure 28 Cut sample to fit into SEM chamber

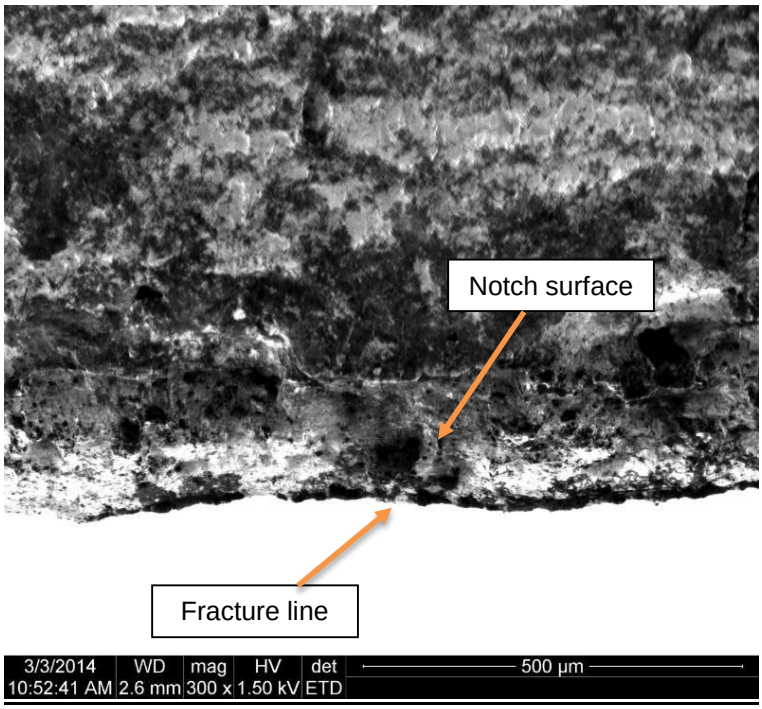

Figure 29 SEM photo of notch and fracture line of sample S4. 300 X.

The above SEM photo captured the surface of the notch and the fracture line of sample S4. Porous structures (dark) could be observed. These were possibly caused by localized corrosion. Also white spots could be observed. These were

possibly corrosion products. The fracture line proves that the fracture has been ductile because local necking can be observed.

The SEM fractograph (100 X) of sample S9 below shows that parts of the material have elongated in direction of loading. This proves that the fracture is ductile.

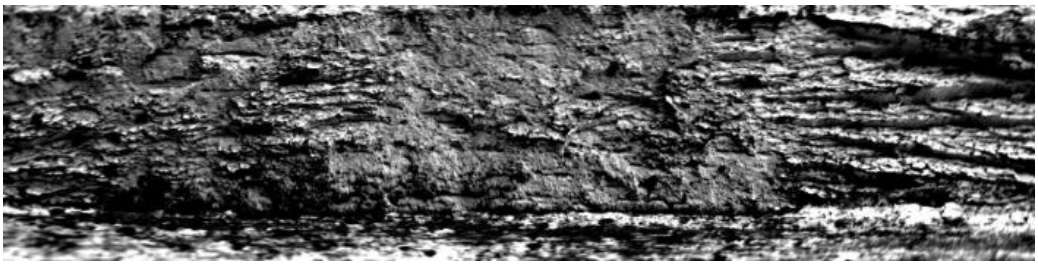

Figure 30 SEM fractograph of sample S9. 100 X.

A more magnified fractograph shows the presence of microvoids (arrow).

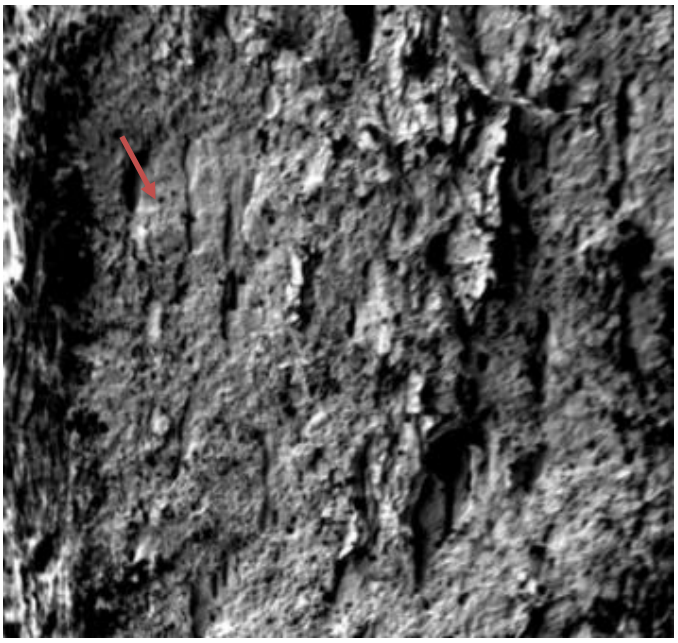

Figure 31 SEM fractograph shows microvoids. 300 X.

4.3. Fatigue Testing Method and Results

Fatigue tests were performed by the MTS testing machine controlled by the Station Manager software in the Corrosion Lab at Seatech. Gripped lengths were consistent with the static tests. The samples were under cyclic tensile loads.

Figure 32 Sample gripped for fatigue testing

4.3.1. Testing Parameters

Samples were tested in different load levels instead of stress levels. All fatigue tests were performed at room temperature under load control at a sinusoidal loading frequency of 5 Hz.

Parameters for fatigue tests are defined as:

1. Stress ratio: R = 0.05. R is defined as the ratio between the maximum load and the minimum load during each fatigue test;
2. Maximum load, P_{max}, is defined for each load level as a percentage (x%) of the mean ultimate load, P_{ult}, calculated from the static tests:

$$P_{max} = x\%P_{ult}; \quad (7)$$

Then, $$P_{min} = RP_{max} = 0.05P_{max}; \quad (8)$$

3. The parameters that need to be entered in the Station Manager software are the mean load and the amplitude of the load:

$$Mean = \frac{P_{max}+P_{min}}{2} = \frac{P_{max}}{2}(1+R) \quad (9)$$

$$Amp = P_{max} - Mean = \frac{P_{max}}{2}(1-R); \quad (10)$$

This calculation was performed for every load level. Five load levels were tested: $P_{max} = 90\%P_{ult}, 80\%P_{ult}, 70\%P_{ult}, 60\%P_{ult,}\ 50\%P_{ult}$. For statistical need, each load level was tested by at least 3 samples.

An Excel™ worksheet was programmed for carrying out these calculations for the mean value and the amplitude of the load.

	A	B	C	D
1				
2			Pult1 =	19.933
3			Pult2 =	21.559
4			Pult3 =	25.323
5			Pult =	22.2716667
6				
7			Load level:	
8	Pmax =	70%	Pult =	15.5901667
9			R =	0.05
10			Mean =	8.1848375
11			Amp =	7.40532917
12				

Figure 33 Excel™ workprogram for calculating fatigue testing parameters

The mean values and amplitudes of 5 different load levels are shown in Table.8.

Table 8 Mean values and amplitudes for 5 different load levels of fatigue testing

Load Level	Mean value (kN)	Amplitude (kN)
90%P_{ult}	10.52	9.52
80%P_{ult}	9.35	8.46
70%P_{ult}	8.18	7.41
60%P_{ult}	7.02	6.35
50% P_{ult}	5.85	5.29

4. Testing frequency was 5 Hz;
5. Fatigue runout was defined as no failure at 1 million (1 X 10^6) cycles.

4.3.2 Fatigue Testing Results

In this section, results of fatigue tests of 16 samples are presented. Due to a mechanical system tuning problem during the tests, negative loads or compression were presented on samples F1, F2, F3, F5, F6, F7, F12, F13, and F14. The MTS testing machine was then tuned for sample F15, F17, F18, F19, F20, F21 and F22. The negative loads might had reduced the fatigue lives of samples because of buckling. All the samples have failed into two pieces at the notch except the runout samples F21 at load level of 60% and F17 at load level of 50%. Most of the fractures are both ductile and brittle. For each sample, following diagram and photos are used to illustrate the results:

1. A diagram of force and displacement as a function of a certain period of time (NOT FOR FULL TIME SPAN);

2. A photo that illustrates the samples' elongation. Two broken pieces are put together and are compared to the other part with original length (101 mm);
3. A photo that illustrates the fracture surface in a macroscopic level. It also indicates the ductile fracture length on the fracture surface. Fractographs of microscopic levels are presented in the next section.

In the end of this section, observations and conclusions are drawn from these results. Also the numbers of cycles to failure are listed.

Fatigue testing results of sample F1 with load level of 90%P_{ult}:

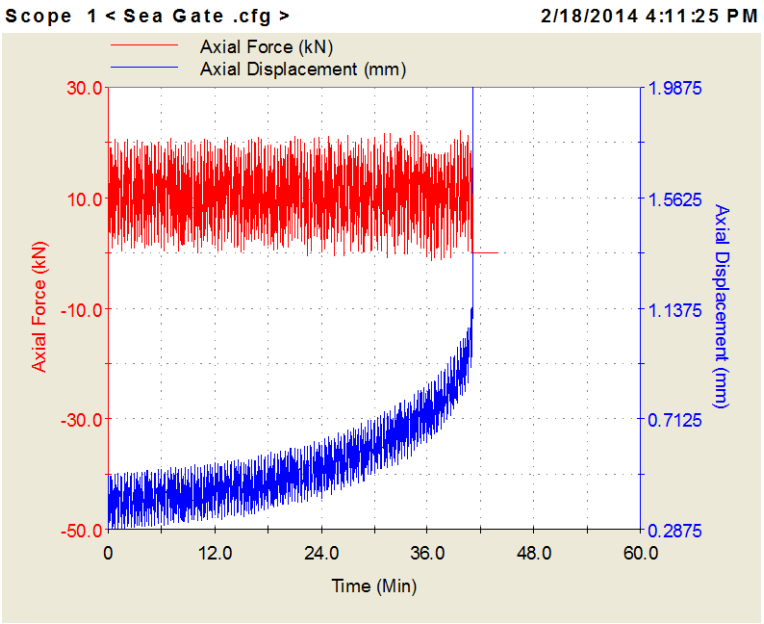

Figure 34 Force and displacement on sample F1 (90%)

Figure 35 Photo of fractured sample F1 (90%)

Fatigue testing results of sample F2 with load level of 90%P_{ult}:

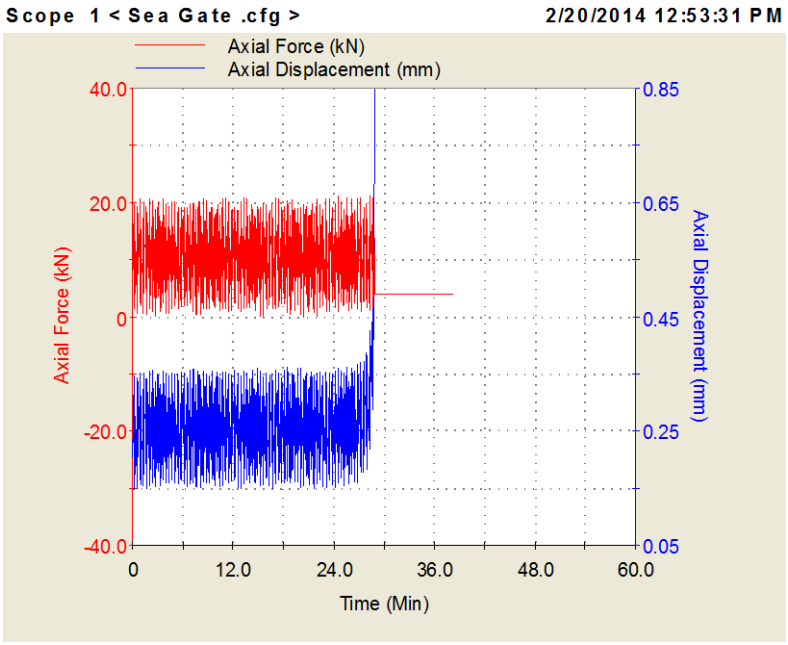

Figure 36 Force and displacement on sample F2 (90%)

Figure 37 Photo of fractured sample F2 (90%)

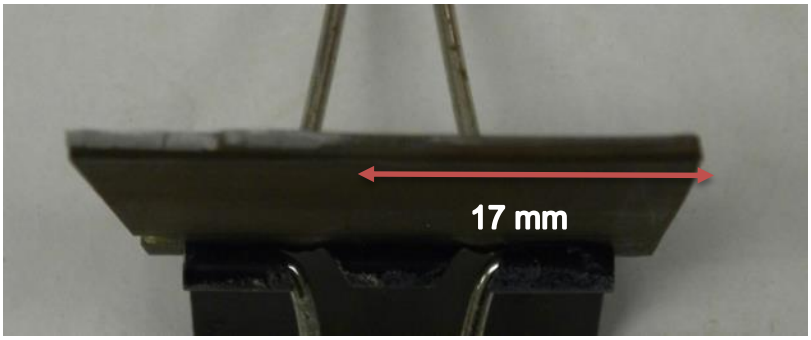

Figure 38 Photo of fracture surface of sample F2 (90%)

Fatigue testing results of sample F3 with load level of 90%P_{ult}:

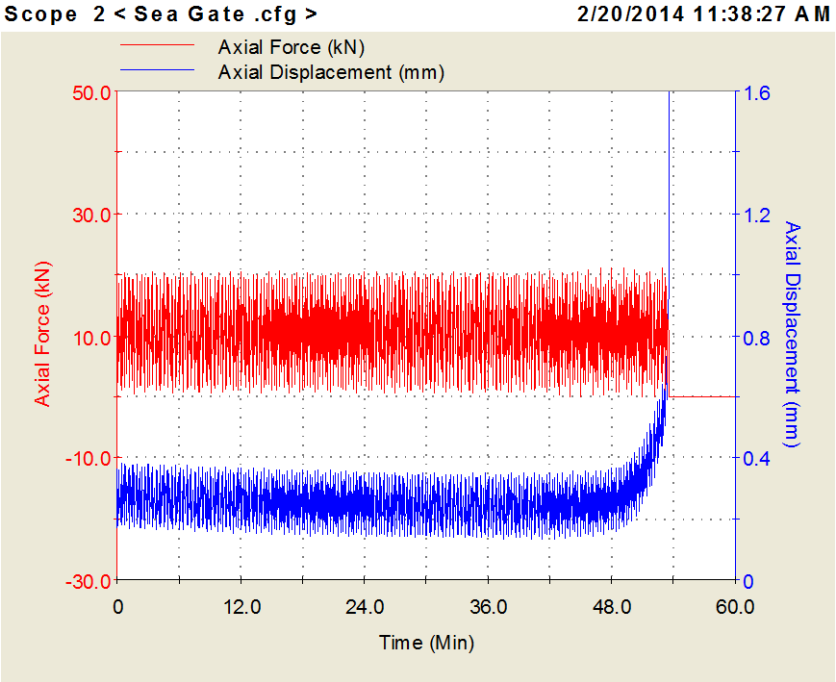

Figure 39 Force and displacement on sample F3 (90%)

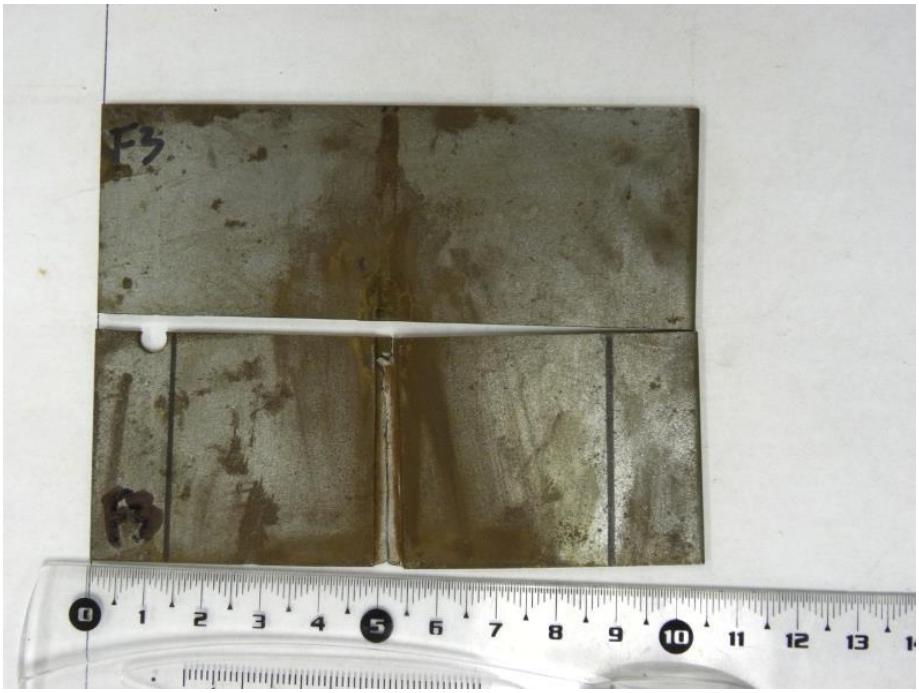

Figure 40 Photo of fractured sample F3 (90%)

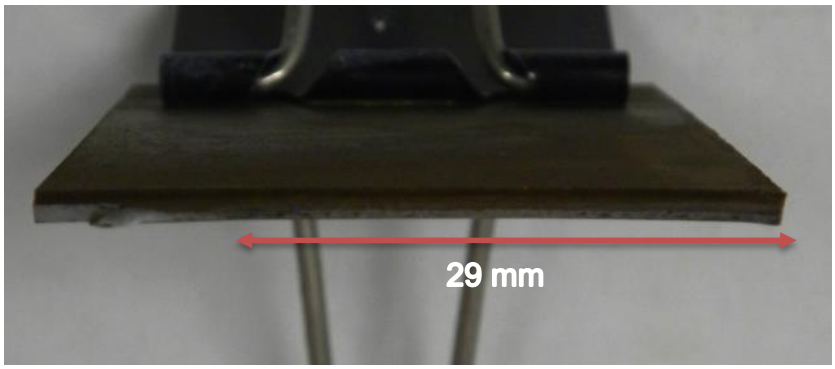

Figure 41 Photo of fracture surface of sample F3 (90%)

Fatigue testing results of sample F19 with load level of 90%P_{ult}:

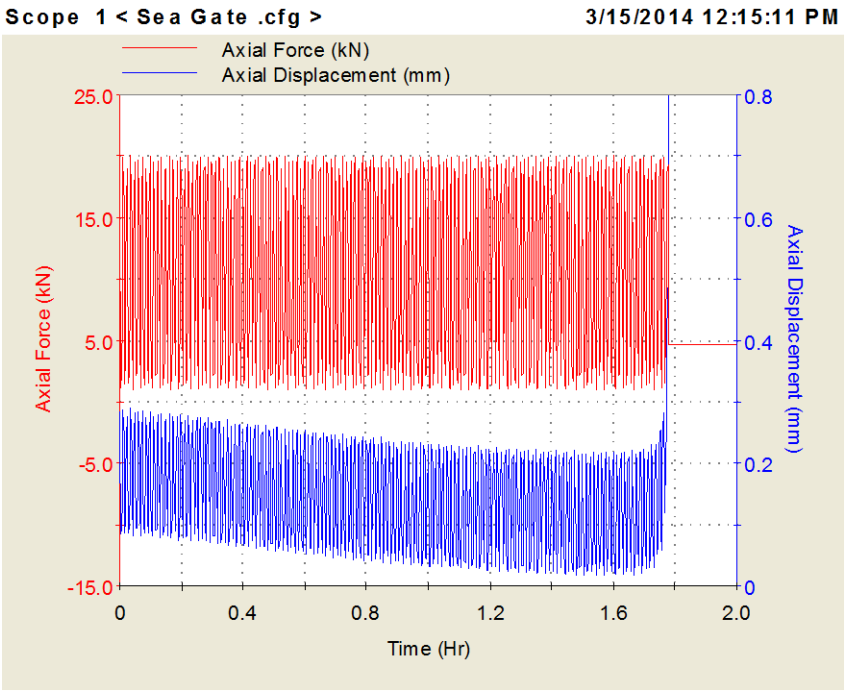

Figure 42 Force and displacement on sample F19 (90%)

Figure 43 Photo of fractured sample F19 (90%)

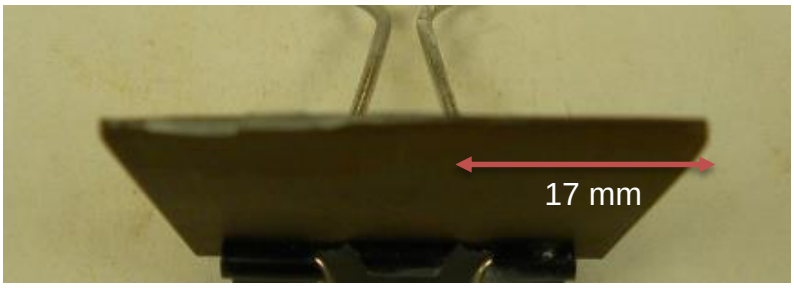

Figure 44 Photo of fracture surface of sample F19 (90%)

Fatigue testing results of sample F5 with load level of 80%P_{ult}:

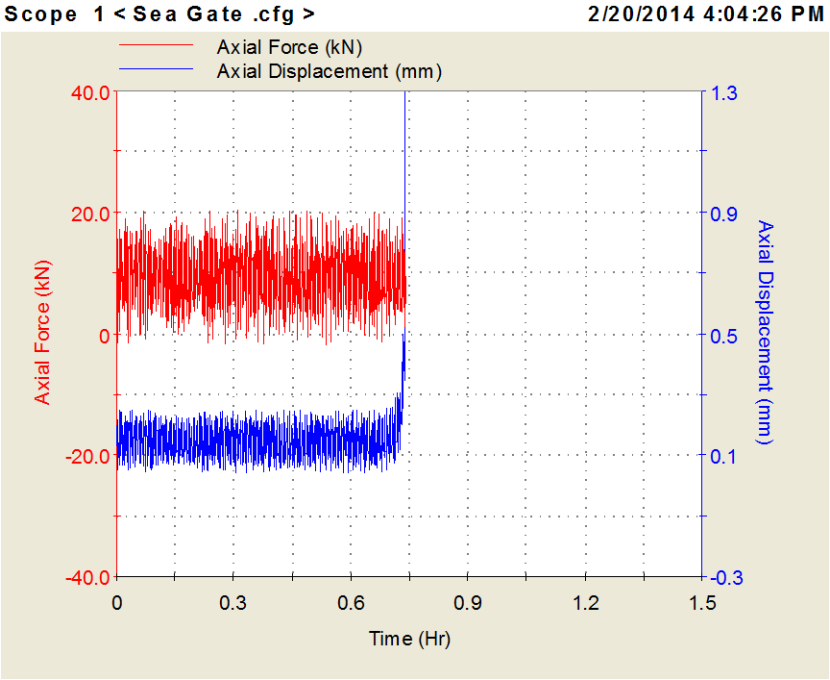

Figure 45 Force and displacement on sample F5 (80%)

Figure 46 Photo of fractured sample F5 (80%)

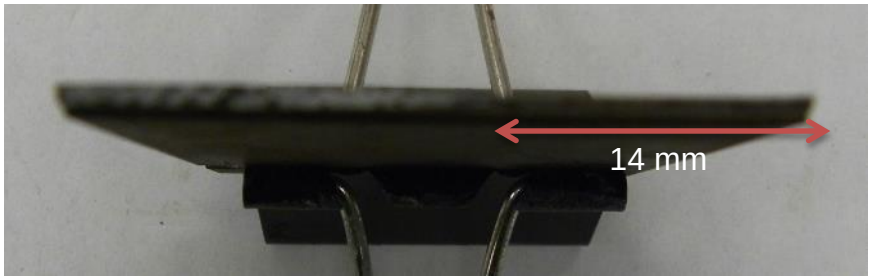

Figure 47 Photo of fracture surface of sample F5 (80%)

Fatigue testing results of sample F6 with load level of 80%P_{ult}:

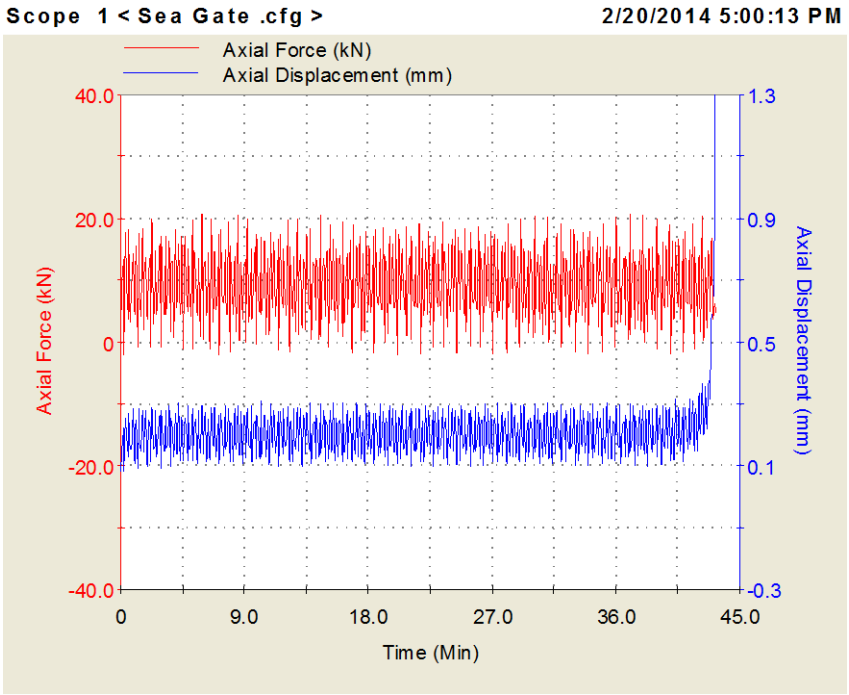

Figure 48 Force and displacement on sample F6 (80%)

Figure 49 Photo of fractured sample F6 (80%)

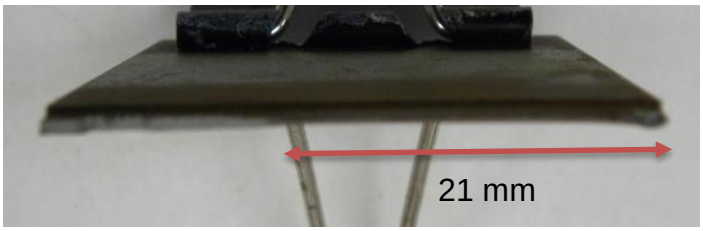

Figure 50 Photo of fracture surface of sample F6 (80%)

Fatigue testing results of sample F7 with load level of 80%P_{ult}:

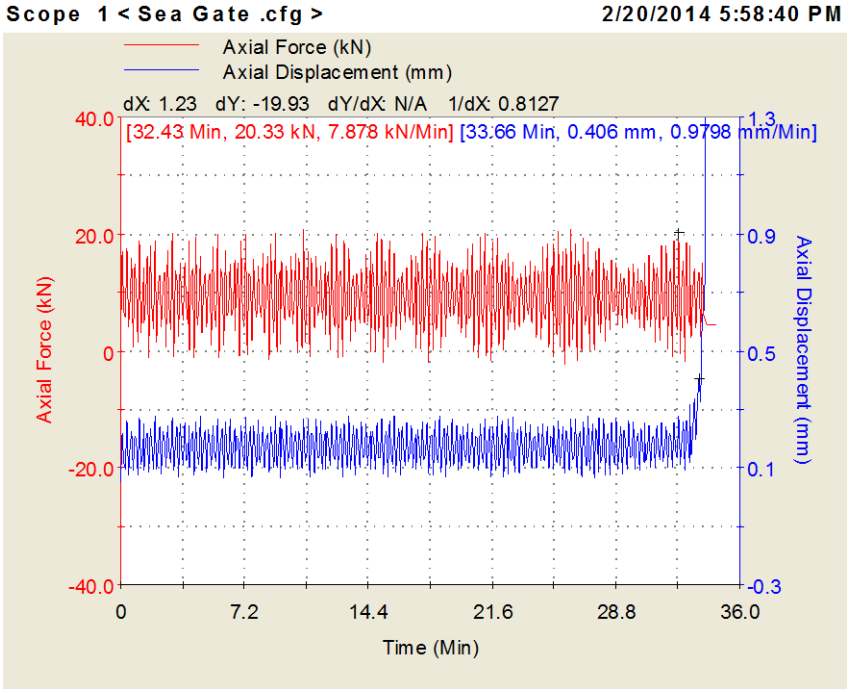

Figure 51 Force and displacement on sample F7 (80%)

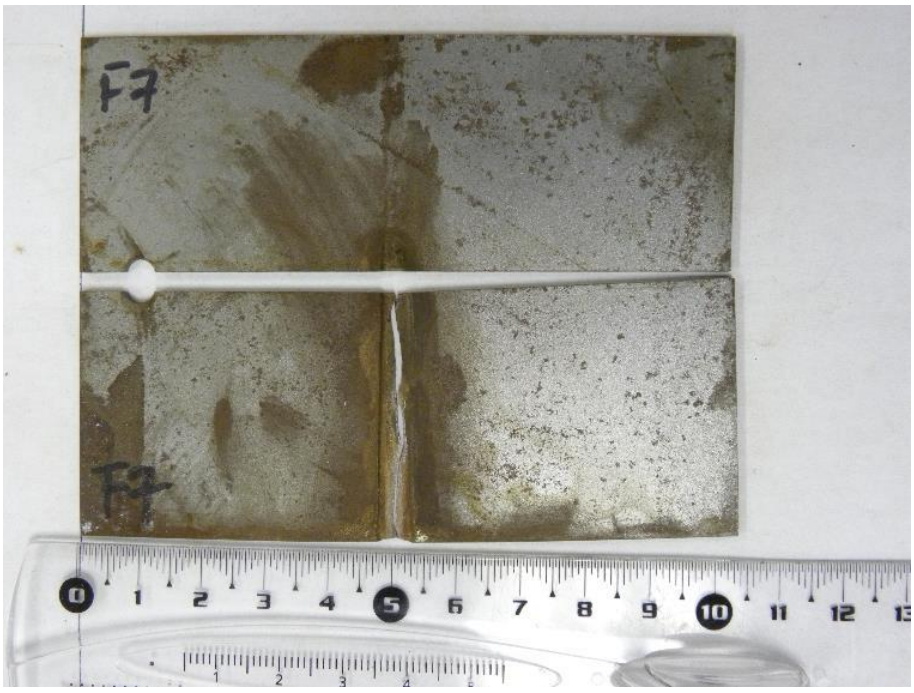

Figure 52 Photo of fractured sample F7 (80%)

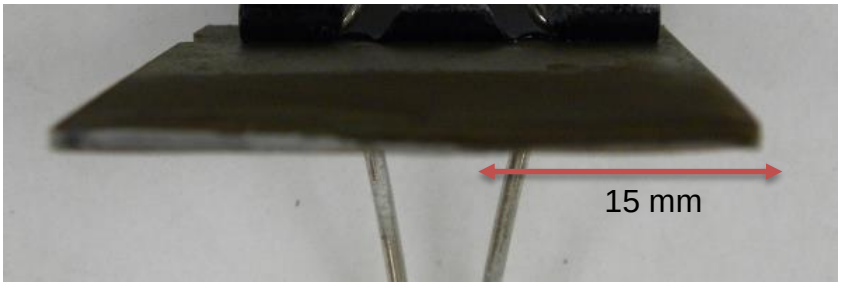

Figure 53 Photo of fracture surface of sample F7 (80%)

Fatigue testing results of sample F20 with load level of 80%P_{ult}:

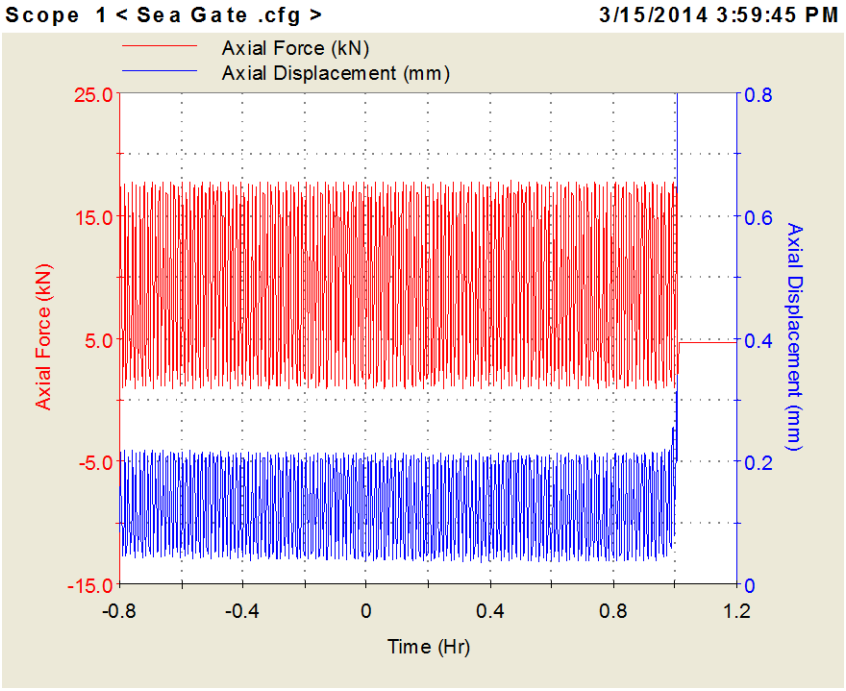

Figure 54 Force and displacement on sample F20 (80%)

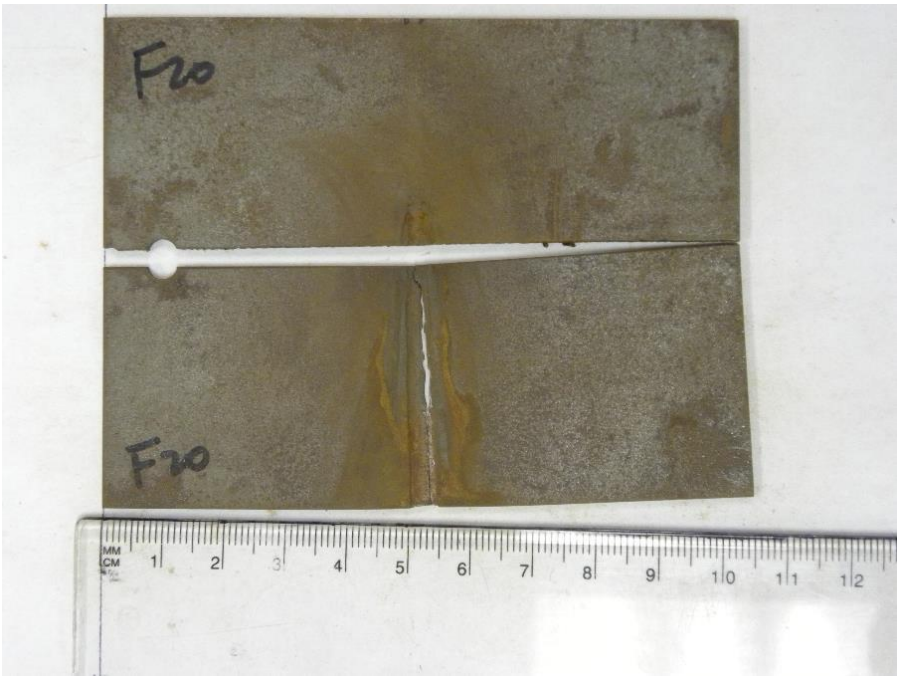

Figure 55 Photo of fractured sample F20 (80%)

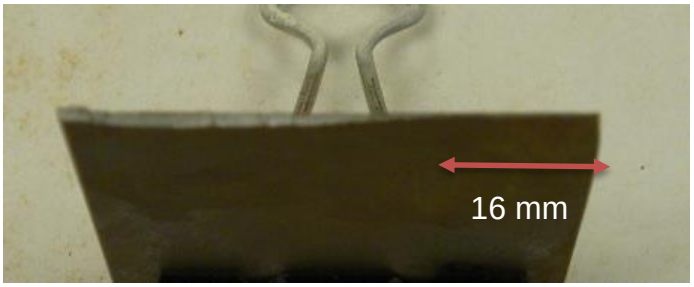

Figure 56 Photo of fracture surface of sample F20 (80%)

Fatigue testing results of sample F12 with load level of 70%P_{ult}:

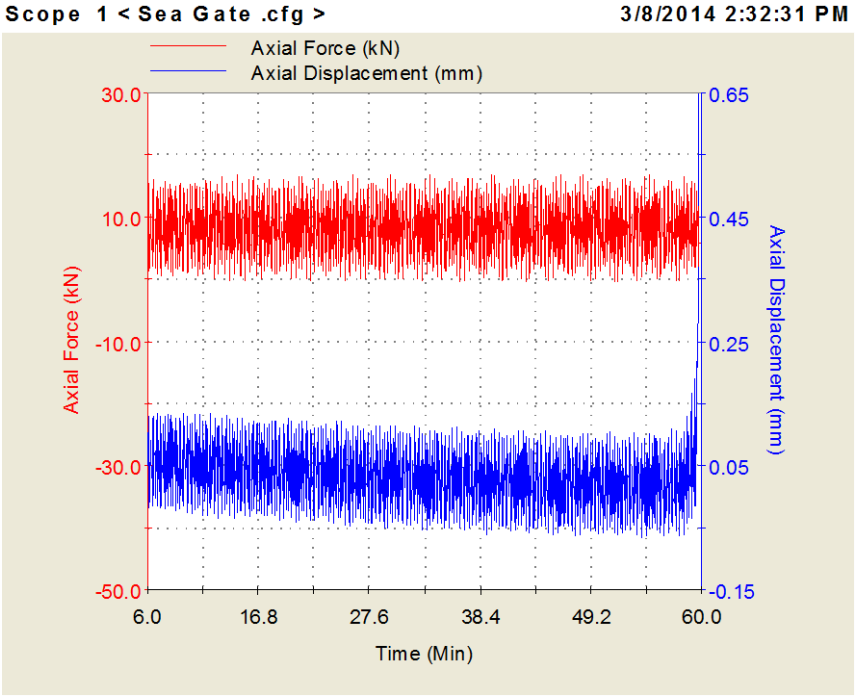

Figure 57 Force and displacement on sample F12 (70%)

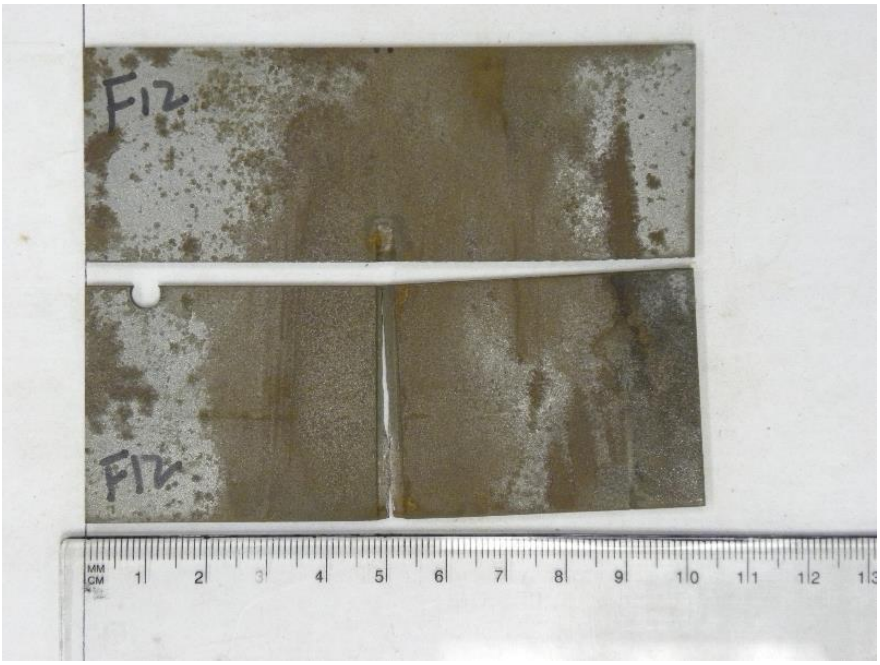

Figure 58 Photo of fractured sample F12 (70%)

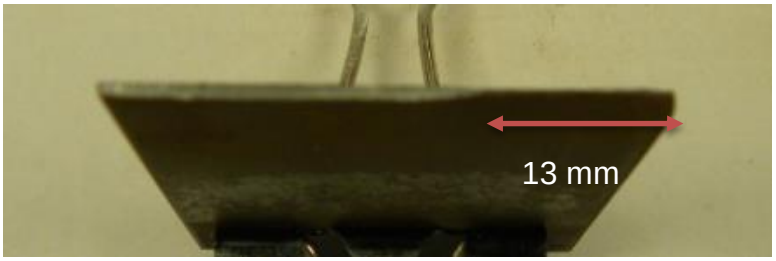

Figure 59 Photo of fracture surface of sample F12 (70%)

Fatigue testing results of sample F13 with load level of 70%P_{ult}:

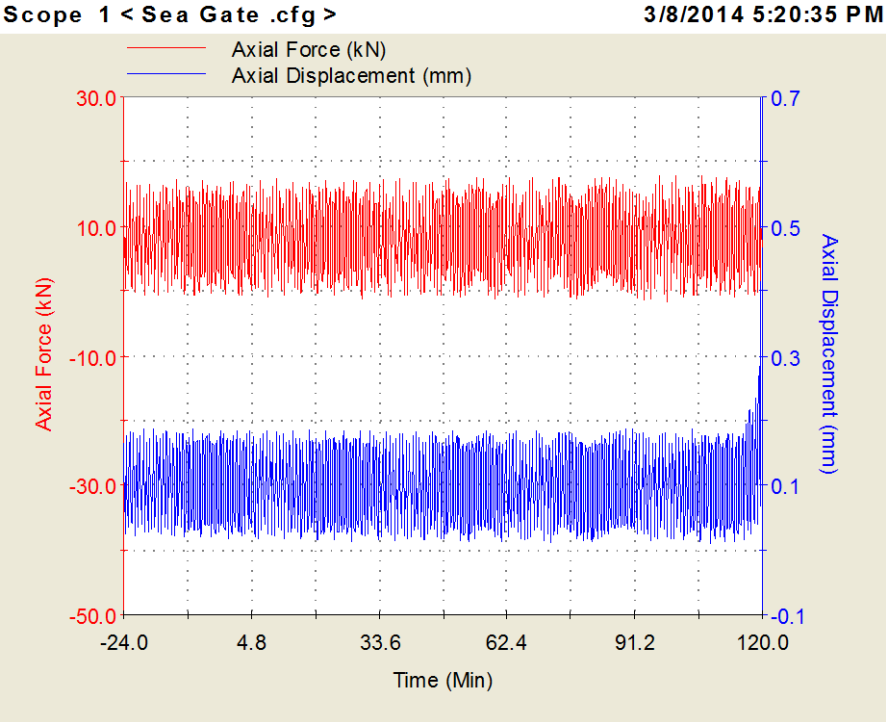

Figure 60 Force and displacement on sample F13 (70%)

Figure 61 Photo of fractured sample F13 (70%)

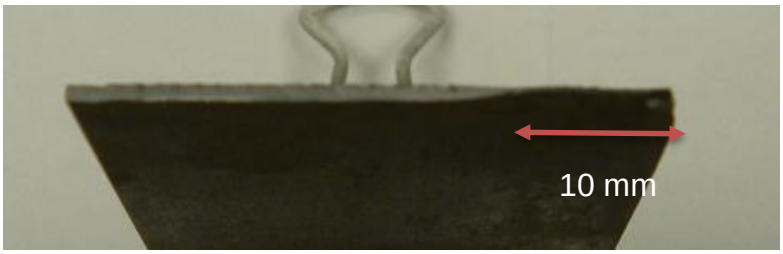

Figure 62 Photo of fracture surface of sample F13 (70%)

Fatigue testing results of sample F14 with load level of 70%P_{ult}:

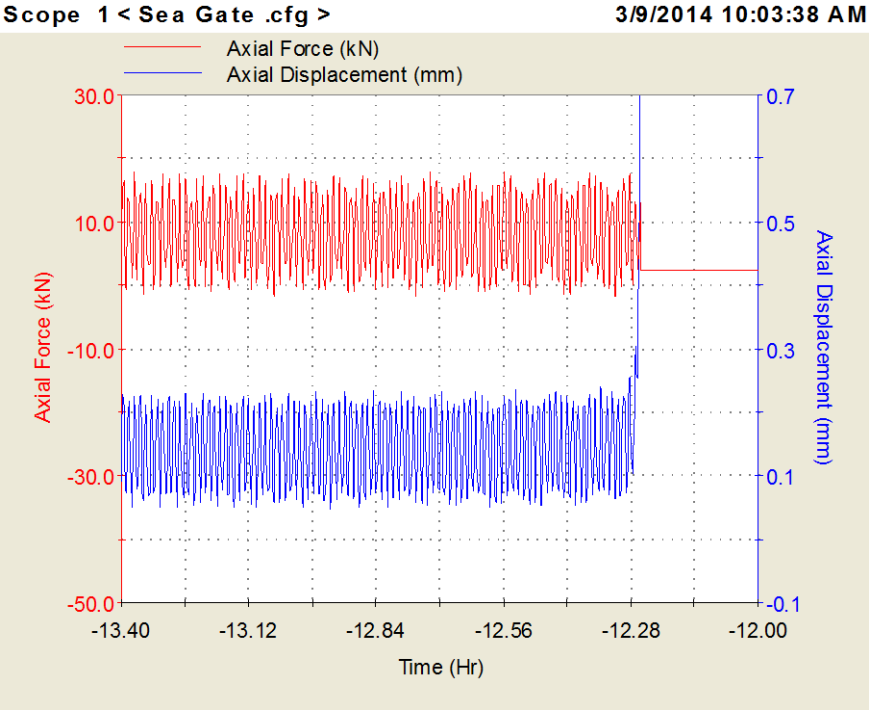

Figure 63 Force and displacement on sample F14 (70%)

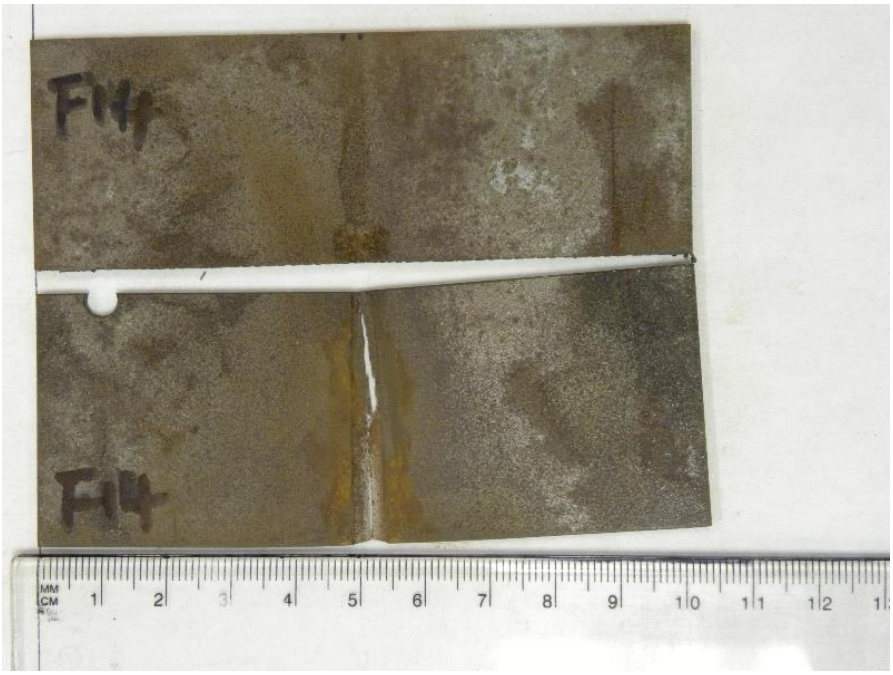

Figure 64 Photo of fractured sample F14 (70%)

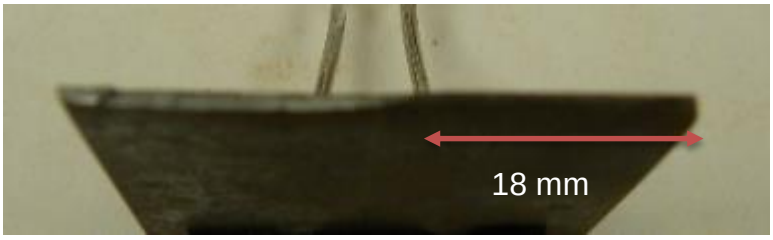

Figure 65 Photo of fracture surface of sample F14 (70%)

Fatigue testing results of sample F22 with load level of 70%P_{ult}:

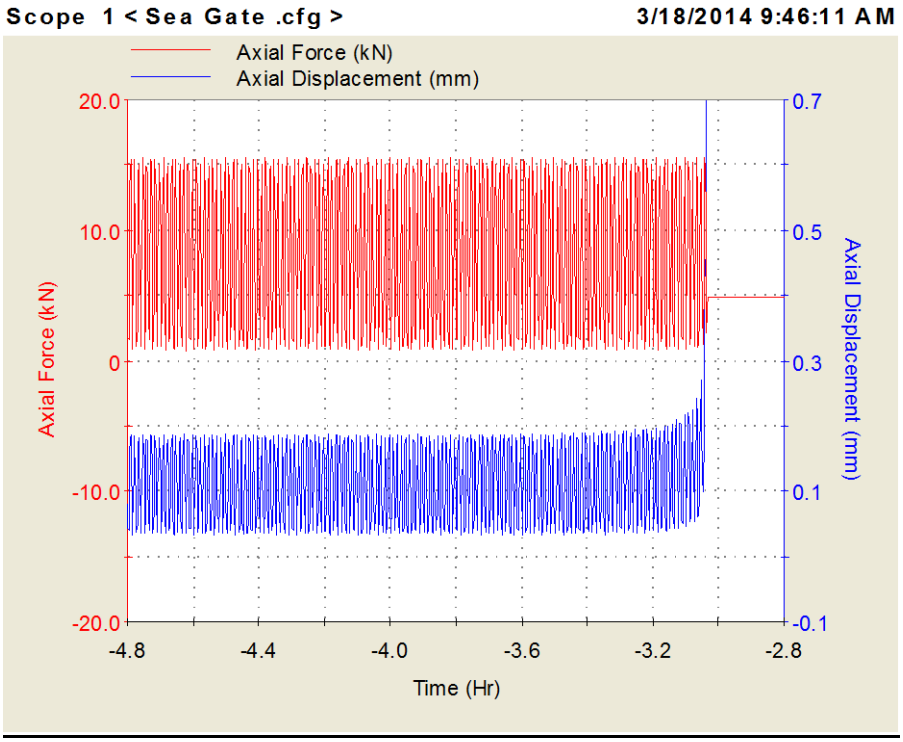

Figure 66 Force and displacement on sample F22 (70%)

Figure 67 Photo of fractured sample F22 (70%)

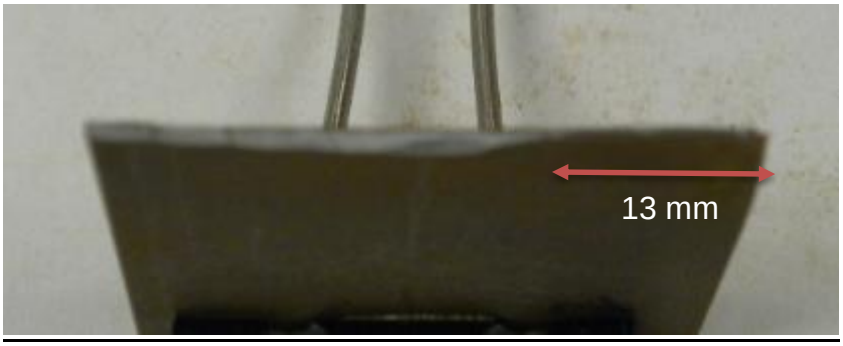

Figure 68 Photo of fracture surface of sample F22 (70%)

Fatigue testing results of sample F15 with load level of 60%P_{ult}:

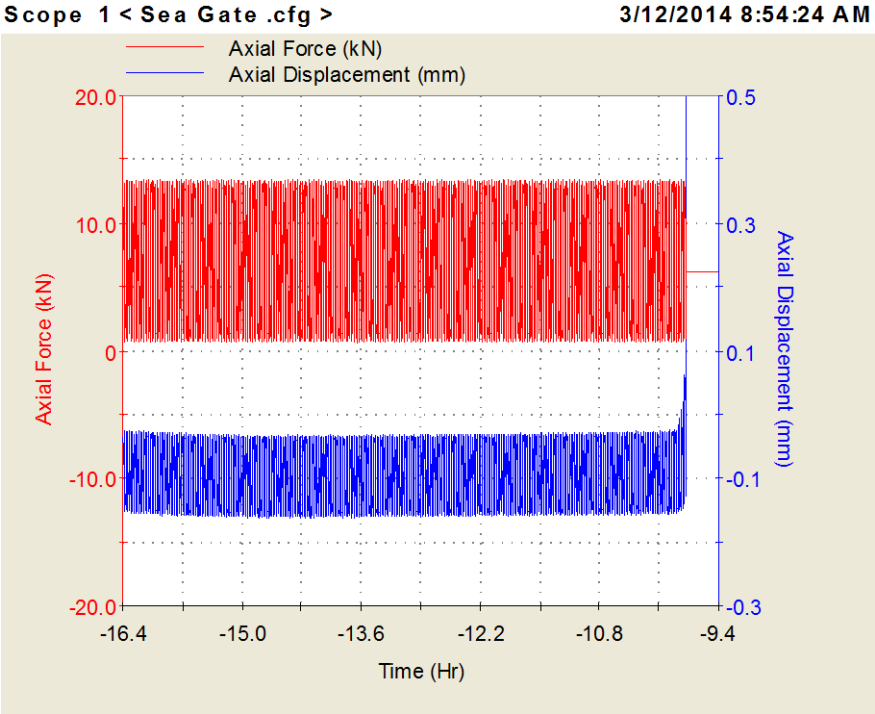

Figure 69 Force and displacement on sample F15 (60%)

Figure 70 Photo of fractured sample F15 (60%)

Figure 71 Photo of fracture surface of sample F15 (70%)

Fatigue testing results of sample F18 with load level of 60%P_{ult}:

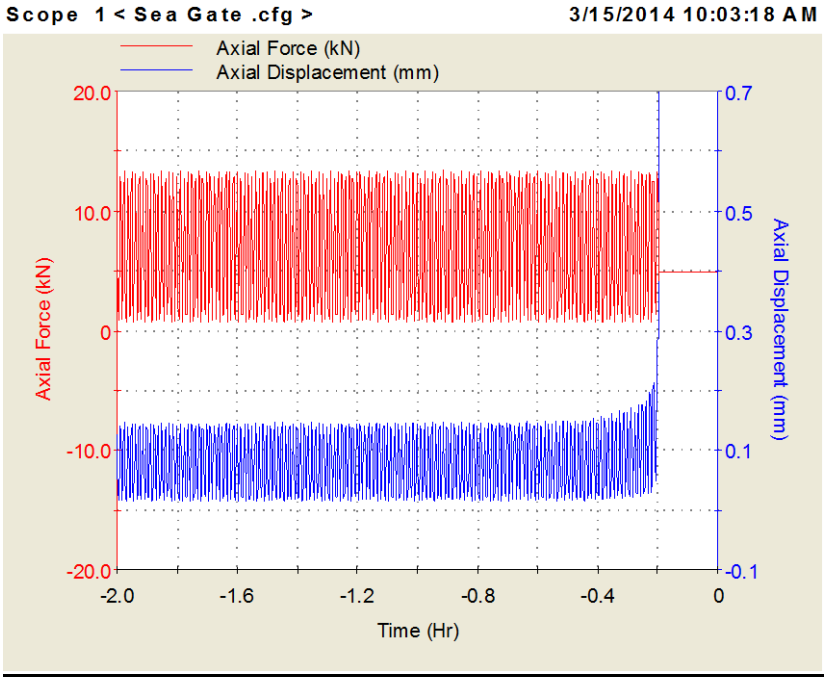

Figure 72 Force and displacement on sample F18 (60%)

Figure 73 Photo of fractured sample F18 (60%)

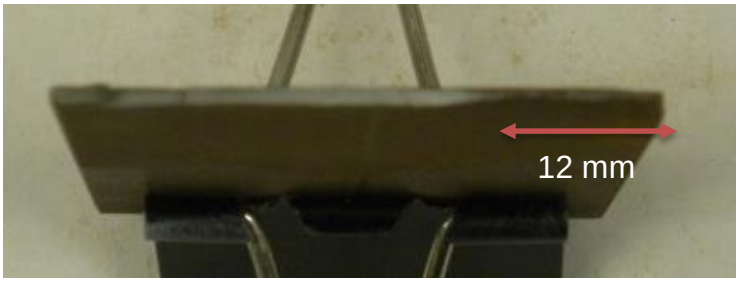

Figure 74 Photo of fracture surface of sample F18 (60%)

Fatigue testing results of sample F21 with load level of 60%P_{ult} (Runout):

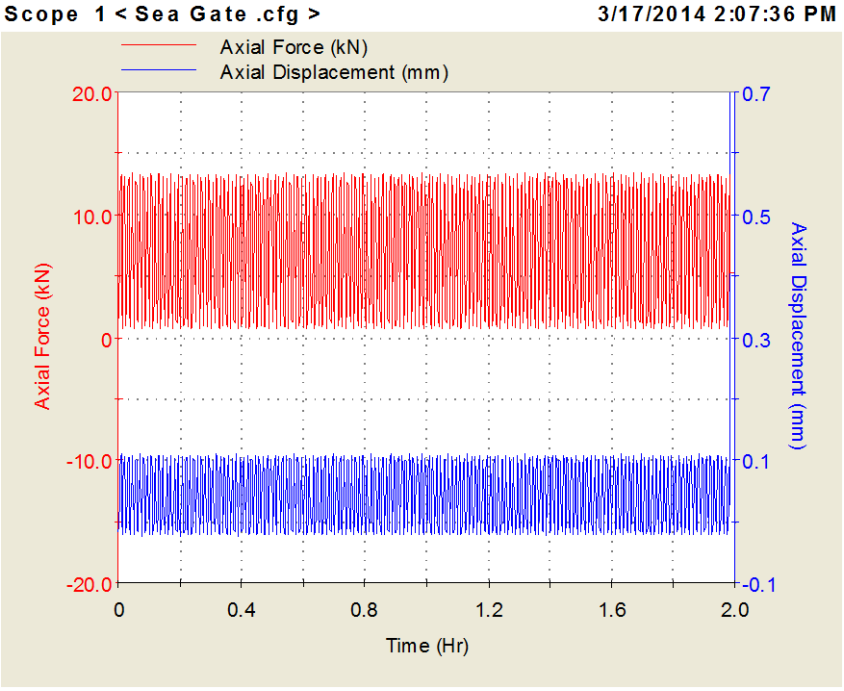

Figure 75 Force and displacement on sample F21 (60%)

Figure 76 Photo of fractured sample F21 (60%)

Fatigue testing results of sample F17 with load level of 50%P_{ult} (Runout):

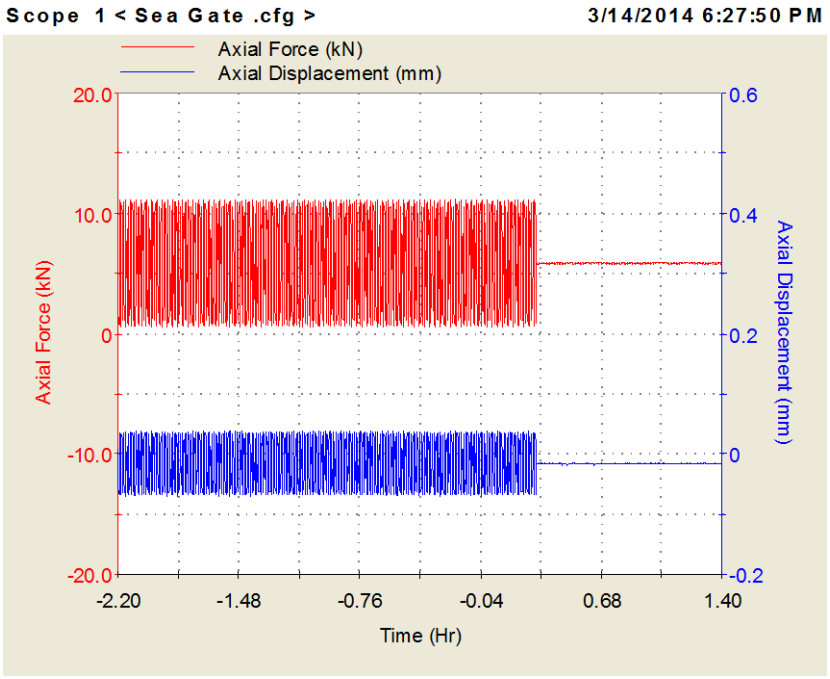

Figure 77 Force and displacement on sample F17 (50%)

Figure 78 Photo of fractured sample F17 (50%)

In the end, the numbers of cycles to failure, the lengths of cross sections that show ductile fracture, the average elongation after testing and the strains are listed in the table below:

Table 9 Numbers of cycles to failure, Ductile fracture length, Average elongation and Strain for each sample after failure

Sample N°	Load Level	Cycles to Failure	Ductile Fracture length (mm)	Average Elongation (mm)	Strain
F1	90%P_{ult}	14,446	39	1.73	1.7%
F2	90%P_{ult}	8,795	17	1.30	1.3%
F3	90%P_{ult}	36,806	29	1.68	1.7%
F19 (Tuned)	90%P_{ult}	33,730	17	2.48	2.5%
F5	80%P_{ult}	14,049	14	2.30	2.3%
F6	80%P_{ult}	13,031	21	1.65	1.6%
F7	80%P_{ult}	10,252	15	1.00	0.9%
F20 (Tuned)	80%P_{ult}	44,836	16	2.11	2.1%
F12	70%P_{ult}	24,949	13	1.48	1.5%
F13	70%P_{ult}	45,222	10	1.33	1.3%
F14	70%P_{ult}	21,152	18	1.27	1.3%
F22 (Tuned)	70%P_{ult}	259,085	13	1.58	1.5%
F15 (Tuned)	60%P_{ult}	170,438	6	1.68	1.7%
F18 (Tuned)	60%P_{ult}	235,969	12	1.70	1.7%
F21 (Tuned)	60%P_{ult}	1 million	No Fracture	0	0.0%
F17(Tuned)	50%P_{ult}	1 million	No Fracture	0	0.0%

“Tuned” behind certain sample numbers means that the machine was tuned for fatigue testing on them.

Some observations can be drawn from above results:

1. All the samples have failed at the location where the notches have been except runout samples F21 and F17;
2. Only sample F1’s fracture surface is all ductile. Necking can be observed on both sides of the sample. Elongation is almost uniform breadthwise;

3. Each of the other broken samples except F1 has both ductile and brittle fracture surfaces. The size of the part that has participated in ductile fracture varies from sample to sample. Necking is only observed on one side of the sample. This has caused uneven elongation. The side with necking has elongated much more than the other side that didn't have necking;
4. Some of the samples haven't elongated as much as the others, such as sample F2, F7, F13 and F14. Moreover, from the above table, we can conclude that samples with larger ductile fracture surfaces often have elongated more;
5. Two runout samples F17 and F21 didn't show any elongation. This was caused by elastic deformation;
6. The elongation had the tendency to decrease as load level decreased.

4.3.3. Microscopic observations of fracture surfaces by SEM

SEM observations have been performed for one sample of each load level.

Fractographs of Sample F2 of load level 90%P_{ult}:

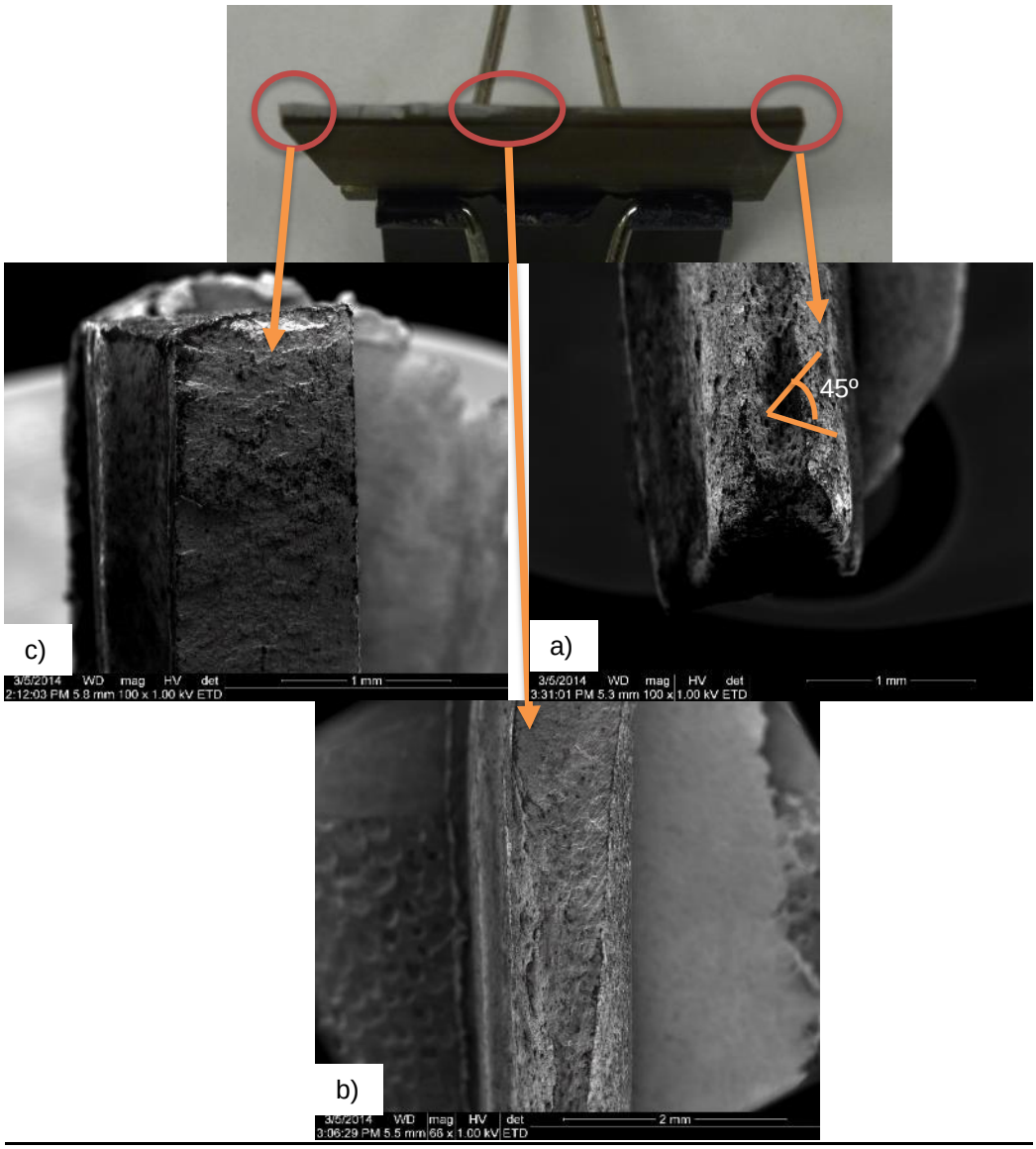

Figure 79 SEM fractographs of sample F2: a) Stage I of fatigue propagation. 100 X. b) Stage II. 66 X. c) Stage III. 100 X.

From the above fractographs, three stages of fractures can be observed:

Stage I: Fig. 79 a) illustrates a slip-plane fracture, extending inward from the surface at approximately 45º to the stress axis. This signifies the initiation of crack.

Stage II: In Fig. 79 b), striations can be observed. This signifies a change of the main fracture plane from one or two shear planes to many parallel plateaus separated by ridges. A fractograph with a higher magnification (100 X) below shows more clearly these fatigue striations. We can also observe the transition from a ductile fracture to a more brittle one.

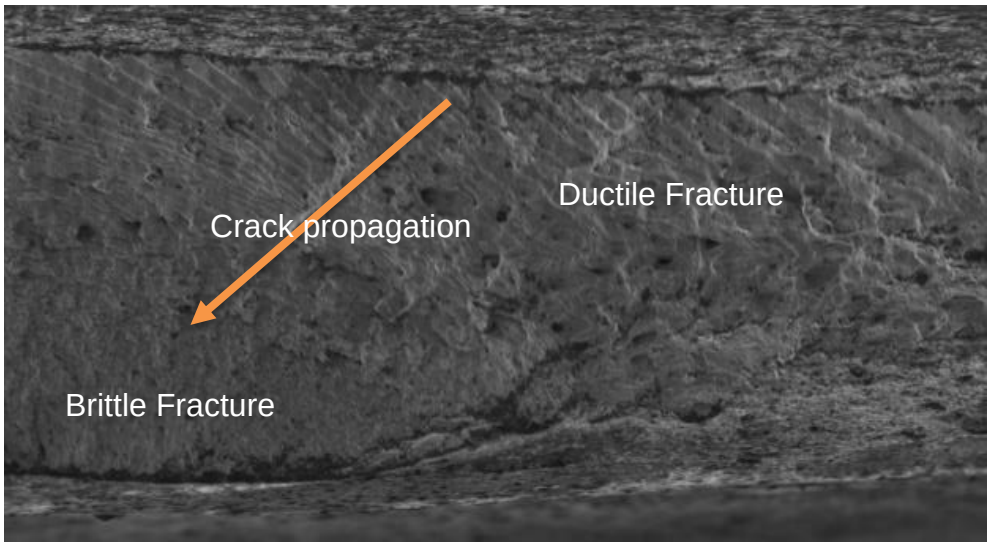

Figure 80 SEM fractograph showing stage II. 100 X.

Stage III: Fig. 79 c) shows a much more brittle fracture. This occurs during the last cycle when sample cannot sustain the load due to a decrease in the cross section.

Fractographs of Sample F6 of load level 80%P_{ult}:

The same stages can be obeserved on the fracture surface of F6. However, there are also some particular features on this surface. Five locations are coded as a), b), c), d), e) as before.

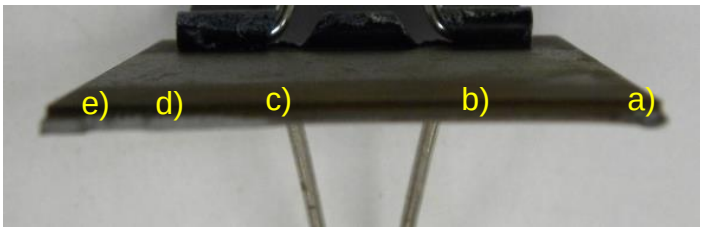

Figure 81 Photo of fracture surface of F6 showing five different locations

1. Fractograph at location a):

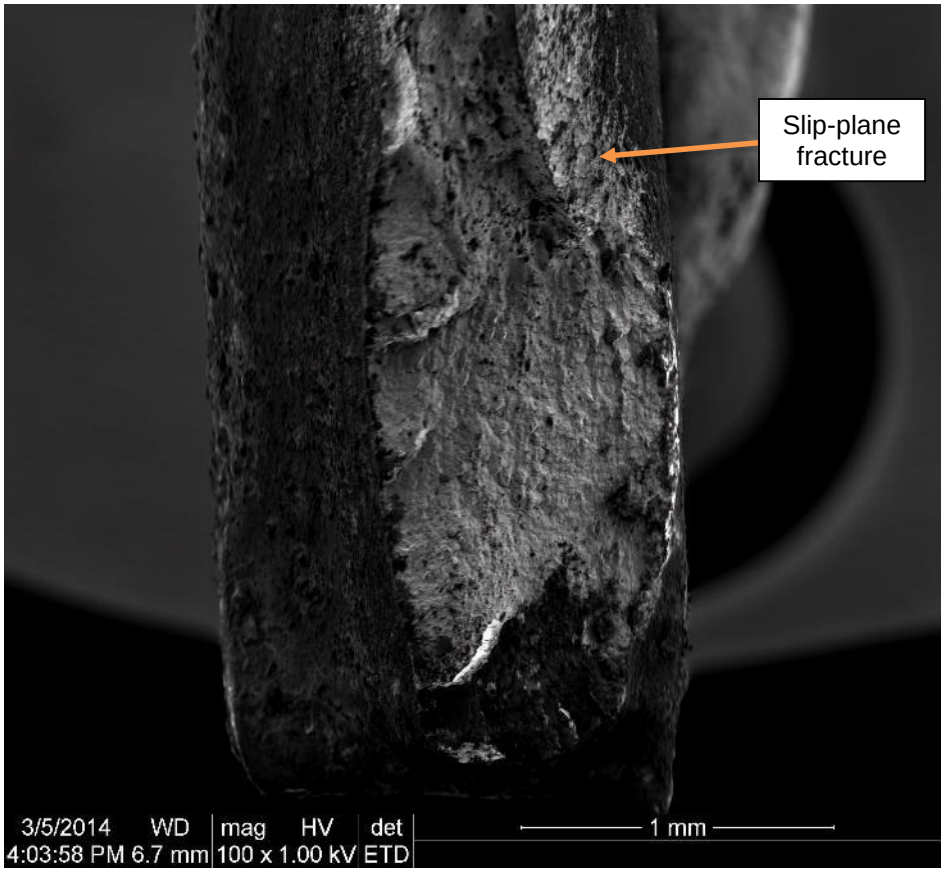

Figure 82 SEM fractograph at location a) of F6. 100 X.

On this fractograph we can see a small area of a combination of brittle and ductile fracture, which has happened even before stage I of ductile fracture. This surface has inconspicuous striations. A slip-plane fracture can be observed in the upper part of the graph, extending inward from the surface at approximately 45º to the stress axis.

2. Fractograph at location b):

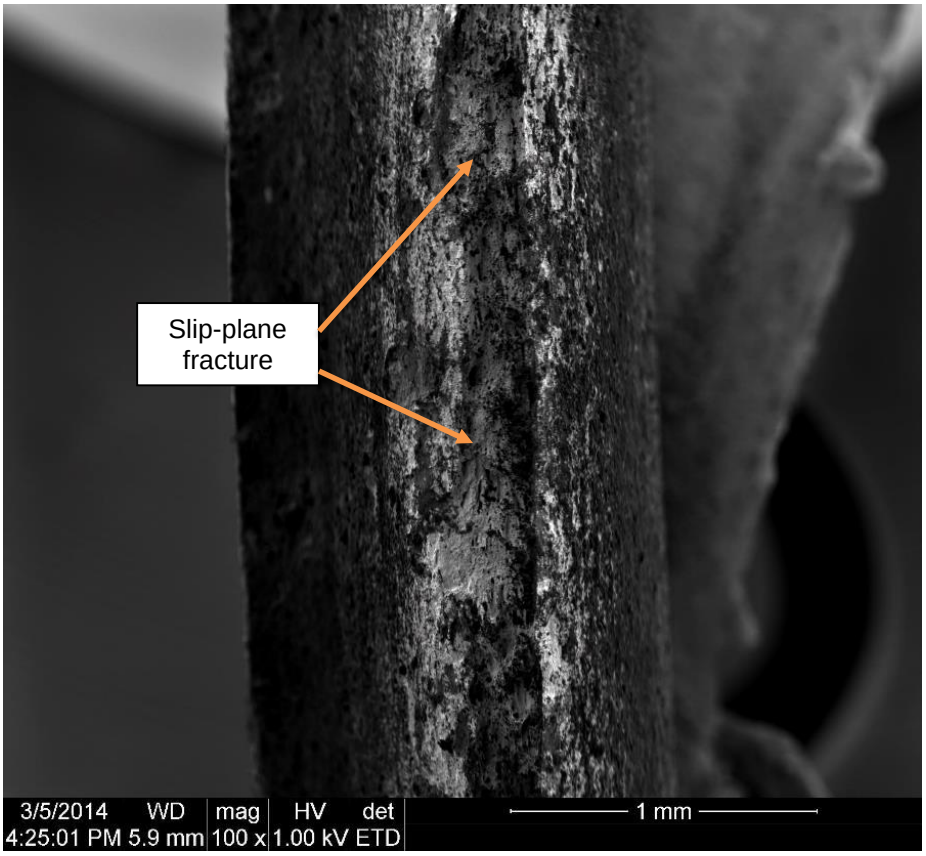

Figure 83 SEM fractograph at location b) of F6. 100 X.

This graph shows typical slip-plane fracture, where the angle caused by stress can be observed.

3. Fractograph at location c):

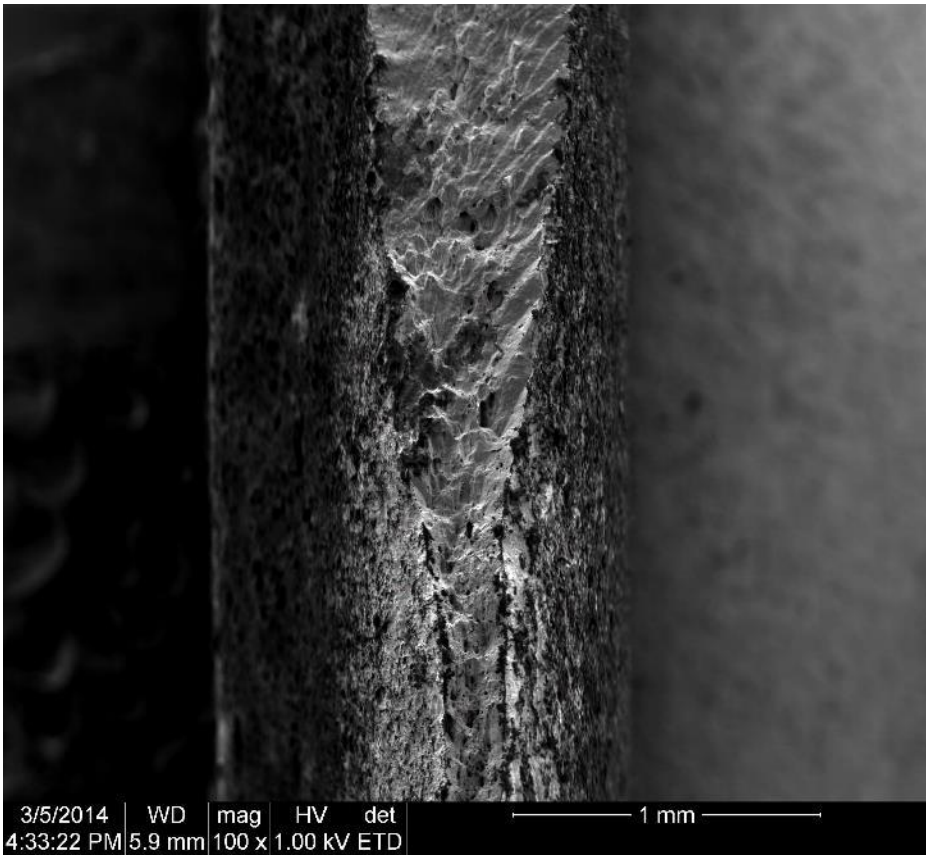

Figure 84 SEM fractograph at location c) of F6. 100 X.

This graph shows the transition from ductile fracture to a more brittle fracture. As before, fatigue striations can be observed.

4. Fractograph at location d):

Different from previous sample F2, this fractograph below illustrates a fracture surface that is parallel to the load provided by the testing machine. This might be caused by localized stress that was perpendicular to the load axis due to deformation.

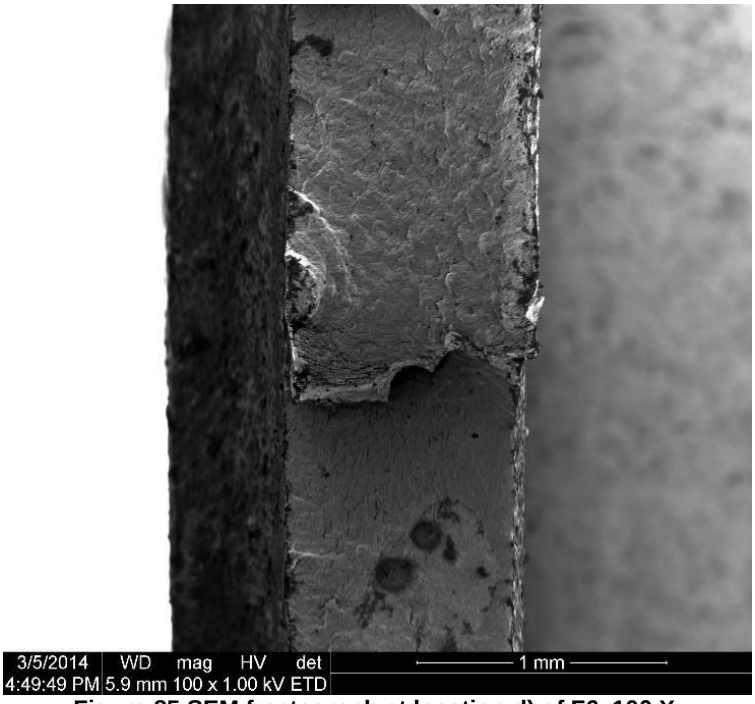

Figure 85 SEM fractograph at location d) of F6. 100 X.

5. Fractograph at location e);

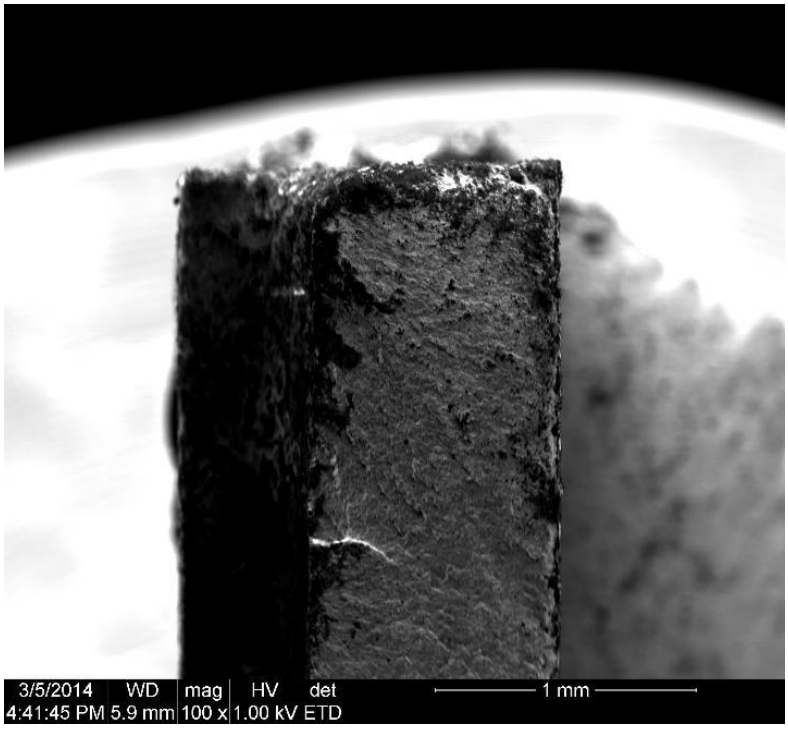

Figure 86 SEM fractograph at location e) of F6. 100 X.

This graph shows a more brittle fracture as in stage III.

Fractographs of Sample F22 of load level 70%P_{ult}:

Three stages can be obeserved on the fracture surface of F22. There are also some particular features on this surface. Three locations are coded as a), b), c).

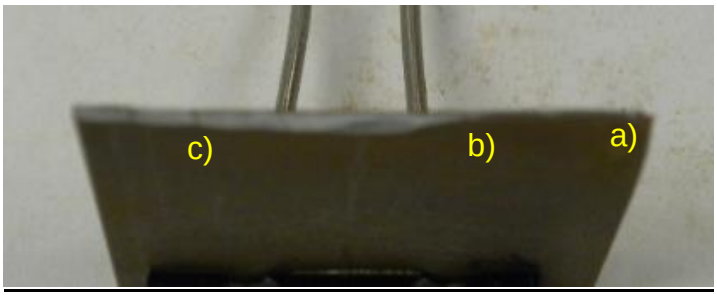

Figure 87 Photo of fracture surface of F22 showing three different locations

1. Fractograph at location a):

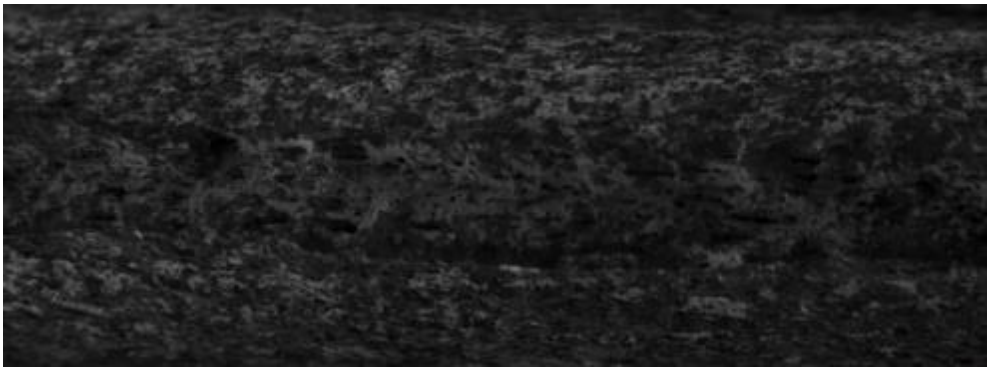

Figure 88 SEM fractograph at location a) of F22. 100 X.

First stage is shown in this fractograph. More microvoids can be observed on this surface than previous ones. The angle caused by stress can also be observed.

2. Fractograph at location b):

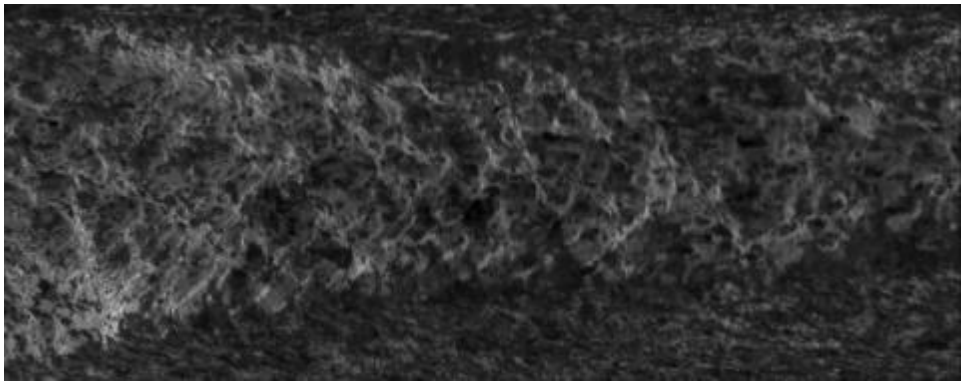

Figure 89 SEM fractograph at location b) of F22. 100 X.

Stage II or the transition between ductile and brittle fracture can be observed here. Different from previous fractographs at this location, the striations on this surface seems to be more disordered and deeper.

3. Fractograph at location c):

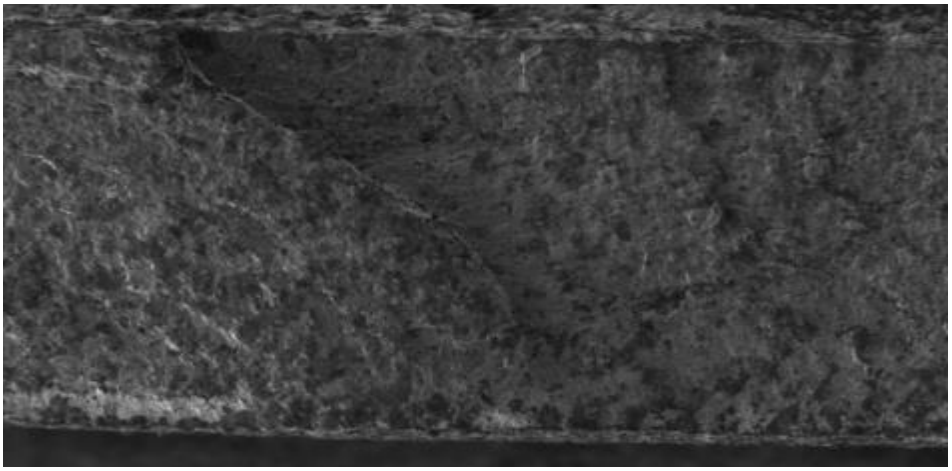

Figure 90 SEM fractograph at location c) of F22. 100 X.

This fractograph shows stage III. A ramp joints two parallel surfaces. It shows evidence of both ductile and brittle fracture.

Fractographs of Sample F15 of load level 60%P_{ult}:

The same three stages can be obeserved on the fracture surface of F15. There are also some particular features on this surface. Three locations are coded as a), b), c).

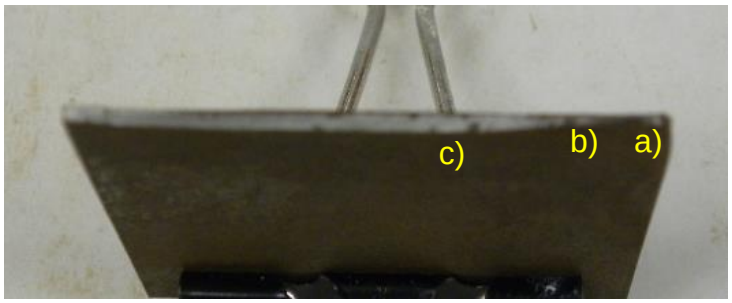

Figure 91 Photo of fracture surface of F15 showing three different locations

1. Fractograph at location a):

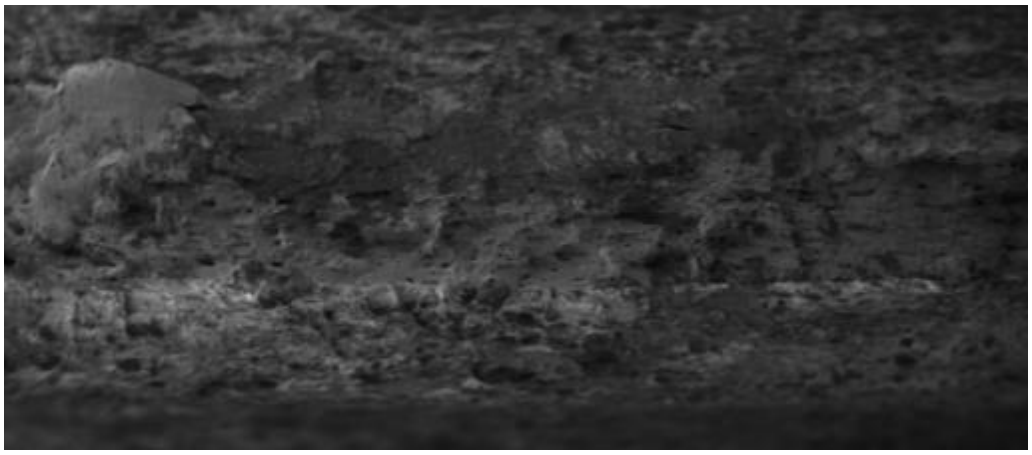

Figure 92 SEM fractograph at location a) of F15. 100 X.

Characteristics such as microvoids and angle caused by stress can be observed in this stage I.

2. Fractograph at location b):

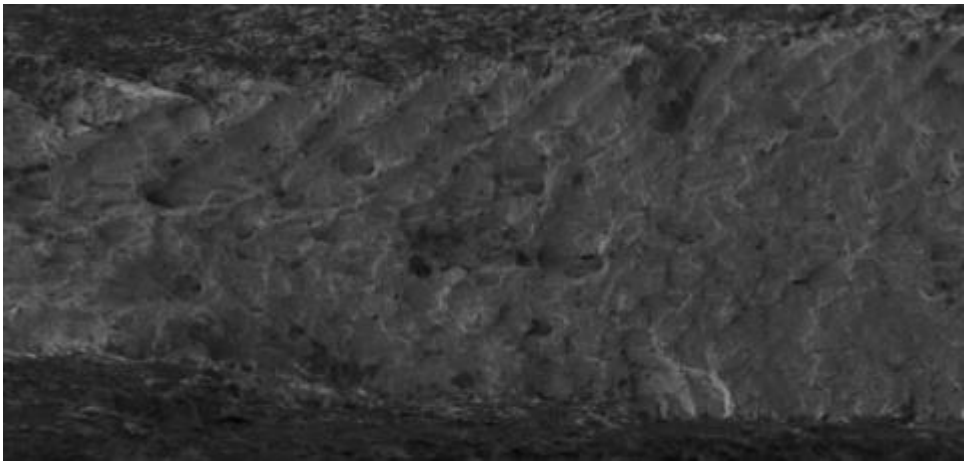

Figure 93 SEM fractograph at location b) of F15. 100 X.

Striations and microvoids can be observed in this stage II. The striations shown above are wider than previous ones.

3. Fractograph at location c):

Figure 94 SEM fractograph at location c) of F15. 100 X.

Stage III presented here (Fig. 94) shows both ductile and brittle fracture.

5. DATA ANALYSIS

Results and data collected in chapter 3 and 4 are analyzed and discussed in this chapter.

5.1. Establishment of S-N Diagrams

From the last chapter, number of cycles to failure as a function of load range is listed in the following table:

Table 10 Number of cycles to failure as a function of load range

Sample N'	Load Level	Load Range, **P** (kN)	Cycles to Failure, **N**
F1	90%P_{ult}	19.04	14,446
F2	90%P_{ult}		8,795
F3	90%P_{ult}		36,806
F19	90%P_{ult}		33,730
F5	80%P_{ult}	16.93	14,049
F6	80%P_{ult}		13,031
F7	80%P_{ult}		10,252
F20	80%P_{ult}		44,836
F12	70%P_{ult}	14.81	24,949
F13	70%P_{ult}		45,222
F14	70%P_{ult}		21,152
F22	70%P_{ult}		259,085
F15	60%P_{ult}	12.69	170,438
F18	60%P_{ult}		235,969
F21 (runout)	60%P_{ult}		> 1 million
F17 (runout)	50%P_{ult}	10.58	> 1 million

The plot of the loads, P as a function of number of cycles, N to failure based on this table is presented below (runout samples were not considered):

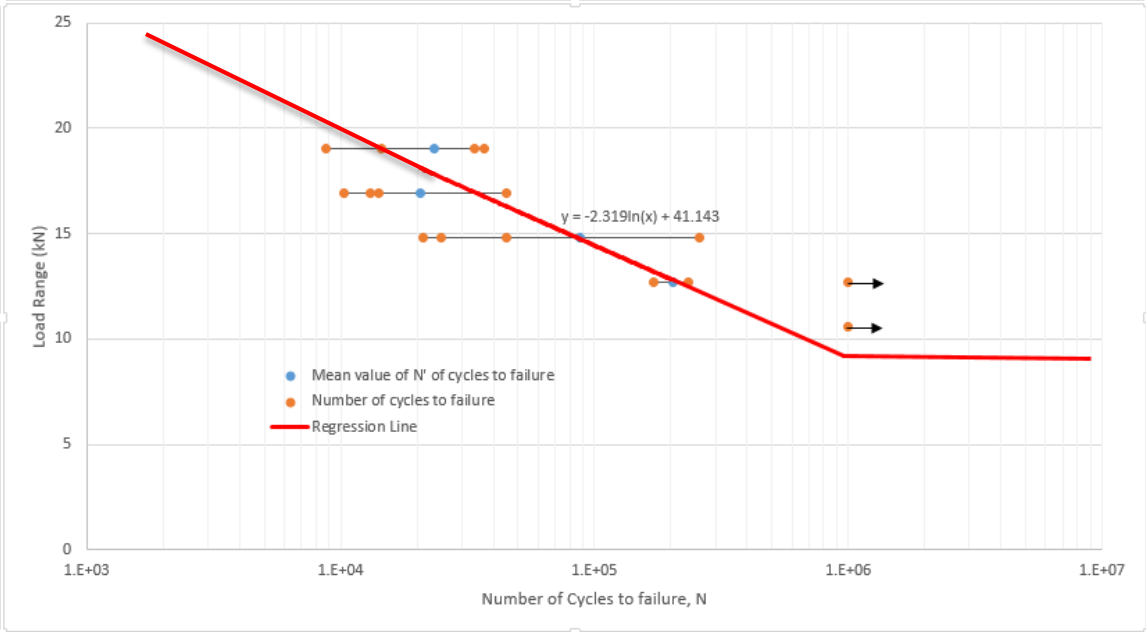

Figure 95 Load-N diagram of corrosion notched A606-04 Type 4 weathering steel samples

The orange points represent the numbers of cycles to failure and blue points represent their mean values. The red regression line was made based on these mean values. As shown in the plot, the regression line is described by the following equations:

$$P = -2.32\ln(N) + 41.14 \qquad (11)$$

$$\text{Or, } P = -5.34\log(N) + 41.14 \qquad (12)$$

To conform to American Association of State Highway and Transportation Officials (AASHTO) fatigue specifications, the load ranges were converted to stress ranges (Table 11, Fig. 96).

To convert loads to stresses, the author referred to Table 4 to calculate first the cross section areas that were subjected to loads and then the stress ranges were calculated. The cross section areas were calculated by multiplying the remaining

thickness in the notch of each sample by 39 mm, which was the width of WS samples.

Mean stress ranges were listed in the last column in Table 11 below [**1**]:

Table 11 Mean stress range converted from loads

Sample	Load Level	Cycles to Failure, **N**	Load Range (kN)	Cross section area (mm^2)	Stress Range (MPa)	Mean Stress Range, **S** (MPa)
F1	90%P_{ult}	14,446	19.04	48.49	392.66	415.81
F2	90%P_{ult}	8,795	19.04	46.02	413.73	
F3	90%P_{ult}	36,806	19.04	43.55	437.20	
F19	90%P_{ult}	33,730	19.04	45.37	419.66	
F5	80%P_{ult}	14,049	16.93	46.67	362.76	365.32
F6	80%P_{ult}	13,031	16.93	44.33	381.91	
F7	80%P_{ult}	10,252	16.93	49.14	344.53	
F20	80%P_{ult}	44,836	16.93	45.5	372.09	
F12	70%P_{ult}	24,949	14.81	42.77	346.27	318.33
F13	70%P_{ult}	45,222	14.81	47.84	309.57	
F14	70%P_{ult}	21,152	14.81	46.28	320.01	
F22	70%P_{ult}	259,085	14.81	49.79	297.45	
F15	60%P_{ult}	170,438	12.69	44.98	282.13	274.05
F18	60%P_{ult}	235,969	12.69	47.71	265.98	
F21	60%P_{ult}	> 1E+06	12.69	47.32	268.17	268.17
F17	50%P_{ult}	> 1E+06	10.58	45.89	230.55	230.55

An S-N diagram based on the numbers of cycles to failure, N and the mean stress ranges, S were established as follows.

As before, the orange points represent the numbers of cycles to failure and blue points represent their mean values. The red regression line was made based on these mean values.

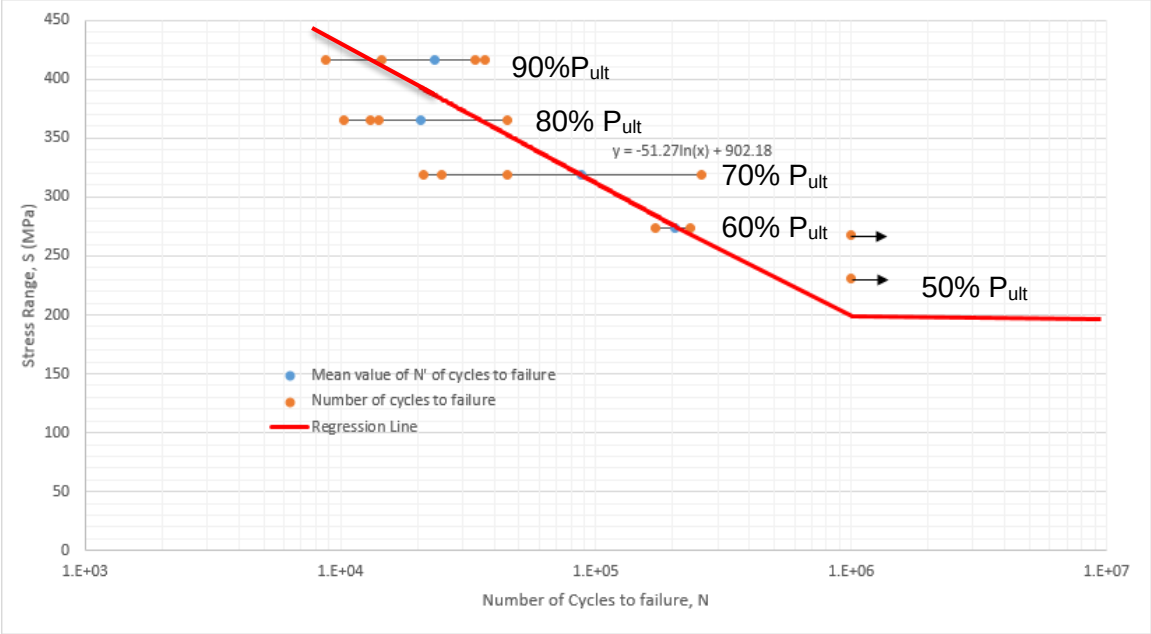

Figure 96 S-N diagram of corrosion notched A606-04 Type 4 weathering steel samples

As shown in the plot, the regression line is described by the following equations:

$$S = -51.27 \ln(N) + 902.18 \qquad (13)$$

Or, $S = -118.07 \log(N) + 902.18$ (14)

It is observed that the mean number of cycles to failure of 80%Pult is a little smaller than that of 90%Pult. This might be caused by the variation of notch geometry and the tuning problem mentioned before.

5.2. Calculation of Fatigue Notch Factor

In AASHTO specifications, the mean regression lines for the sets of data points were calculated by the least-square method using equation below [**1**]:

$$logN = b - m\,logS \quad (15)$$

AASHTO fatigue specifications is shown in table below.

Table 12 Regression analysis and fatigue notch factor of AASHTO fatigue specifications

Category	Regression Coefficient		Stress Range at 500,000 Cycles (MPa)	Fatigue Notch Factor K_f
	Intercept, b	Slope, m		
A	13.785	3.178	350	1.00
B	13.696	3.372	235	1.49
C*	12.681	3.097	180	1.95
C	12.763	3.25	149	2.35
D	12.177	3.071	129	2.72
E	11.886	3.095	100	3.51
E’	11.849	3.2	83.5	4.19

According to Equation (4) and (14), the fatigue notch factor due to the corrosion process in this thesis study can be calculated as:

The stress range of corrosion notched A606-04 Type 4 weathering steel sample at 500,000 cycles is:

$$S_{ws,500000} = -118.07\log(500000) + 902.18 \quad (16)$$

Therefore;

$$S_{ws,500000} = 229.30\ MPa \quad (17)$$

The percentage of decrease from category A is: $\frac{(350\ MPa - 229.30\ MPa)}{350\ MPa} = 34.49\%$.

The fatigue notch factor of corrosion notched A606-04 Type 4 weathering steel is:

$$K_{f,ws} = \frac{f_{rA}}{f_{r1}} = \frac{S_{rA}}{S_{ws,500000}} = \frac{350}{229.30} = 1.53 \quad (18)$$

$$K_{f,ws} = 1.53 \quad (19)$$

Where, $f_{rA} = S_{rA} = 350\ MPa$ is the reference stress at 500,000 cycles of category A.

By comparing $K_{f,ws}$ with Table 12, we have $1.49 < K_{f,ws} < 1.95$. Therefore, the corrosion notched A606-04 Type 4 weathering steel in this thesis study exhibited the fatigue strength between Category B and C*, and also a decrease of fatigue strength of 34.49% compared to category A rolled beam. This fatigue strength is closer to that of Category B than Category C*.

5.3. Weibull Analysis

Weibull analysis was performed in this thesis study for reliability assessment. This is especially important when only limited number of samples were tested. This was the case in this thesis study. Only three or four samples were tested for each load level. The values of the Weibull parameters provide information for classifying failure modes and provide insight towards increasing reliability [**14**].

The Weibull reliability function which describes the probability of survival can be written as [**14**]:

$$R(X) = \exp[-(\frac{X}{\eta})^{\beta}] \quad (20)$$

Its complement, the Cumulative Distribution Function (CDF) or unreliability function *F(X)*, describes the population that will fail by a certain period of time. Therefore, *R(X) = 1 – F(X)*. It can be expressed as:

$$F(X) = 1 - \exp[-(\frac{X}{\eta})^{\beta}] \quad (21)$$

Where

X = any random number; for example, load in static tests or number of cycles to failure in fatigue test.

β = shape parameter of the distribution.

η = scale parameter.

Equation 21 above outlines the two parameter Weibull distribution (2P-Weibull). A commercial software for Weibull analysis was used to perform the calculation of 2P-Weibull distribution and the plot of CDF and reliability function.

Weibull data for both the static tests and fatigue tests is shown in the table below:

Table 13 Weibull data

Static Test				
Sample N°	Load, X (kN)	Shape Parameter, β	Scale Parameter, η	Reliability, R(X)
S4	19.933	8.219	23.431	0.814
S7	21.559			0.604
S9	25.323			0.151
Fatigue Test				
Sample N°	Cycles, X	Shape Parameter, β	Scale Parameter, η	Reliability, R(X)
F2-90%P_{ult}	8,795	1.515	27,322	0.836
F1-90%P_{ult}	14,446			0.683
F19-90%P_{ult}	33,730			0.253
F3-90%P_{ult}	36,806			0.208
F7-80%P_{ult}	10,252	1.814	22,167	0.781
F6-80%P_{ult}	13,031			0.683
F5-80%P_{ult}	14,049			0.646
F20-80%P_{ult}	44,836			0.028
F14-70%P_{ult}	21,152	1.013	79,913	0.771
F12-70%P_{ult}	24,949			0.735
F13-70%P_{ult}	45,222			0.570
F22-70%P_{ult}	259,085			0.037
F15-60%P_{ult}	170,438	0.908	712,410	0.761
F18-60%P_{ult}	235,969			0.693
F21-60%P_{ult}	1000,000 (Runout)			0.256

In the above table, larger value of shape parameter indicates less scatter in test data. A larger shape parameter also indicates that the corresponding scale parameter is closer to the mean value of test data.

R(X) in the last column represents the percentage of the population that will not fail at a certain load or number of cycles, *X*.

For the last set of data of 60% P_{ult}, sample F21 was included in the analysis as a non-failed sample. A maximum likelihood analysis method was performed for this reason. For other data, a rank regression on *X* method was used. Weibull analysis wasn't performed for load level of 50% P_{ult} since there was only one data point.

Weibull plots are shown in the following figures:

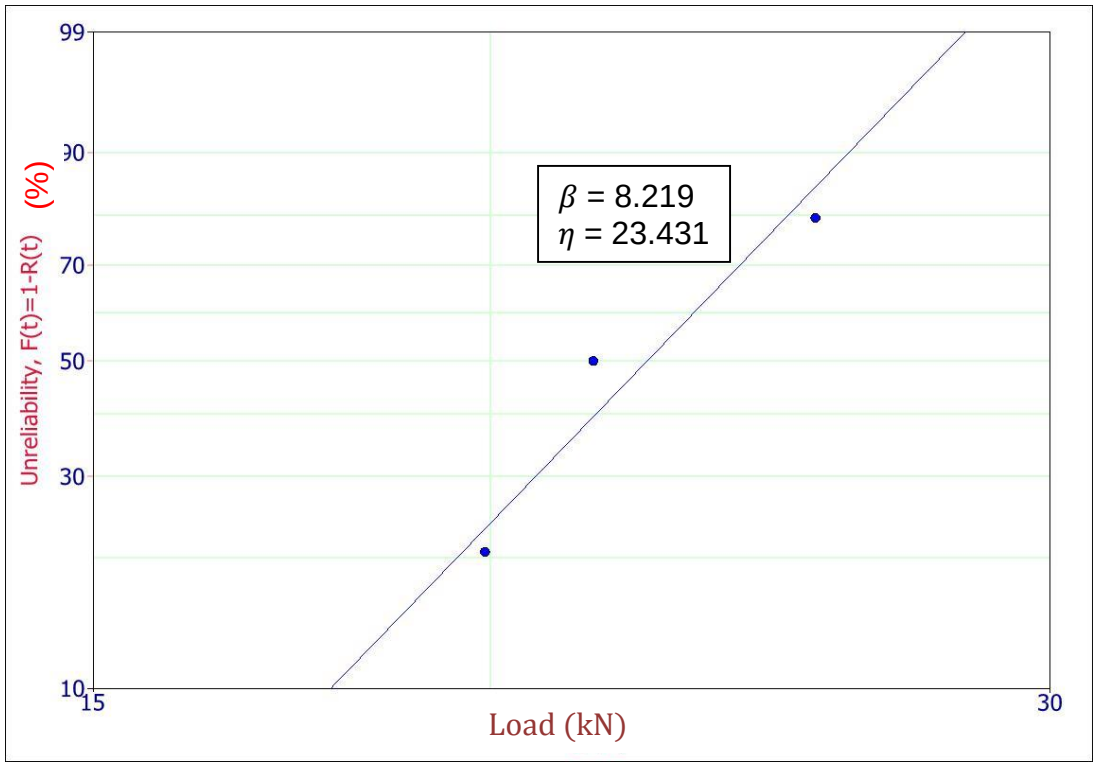

Figure 97 Weibull analysis of static tests

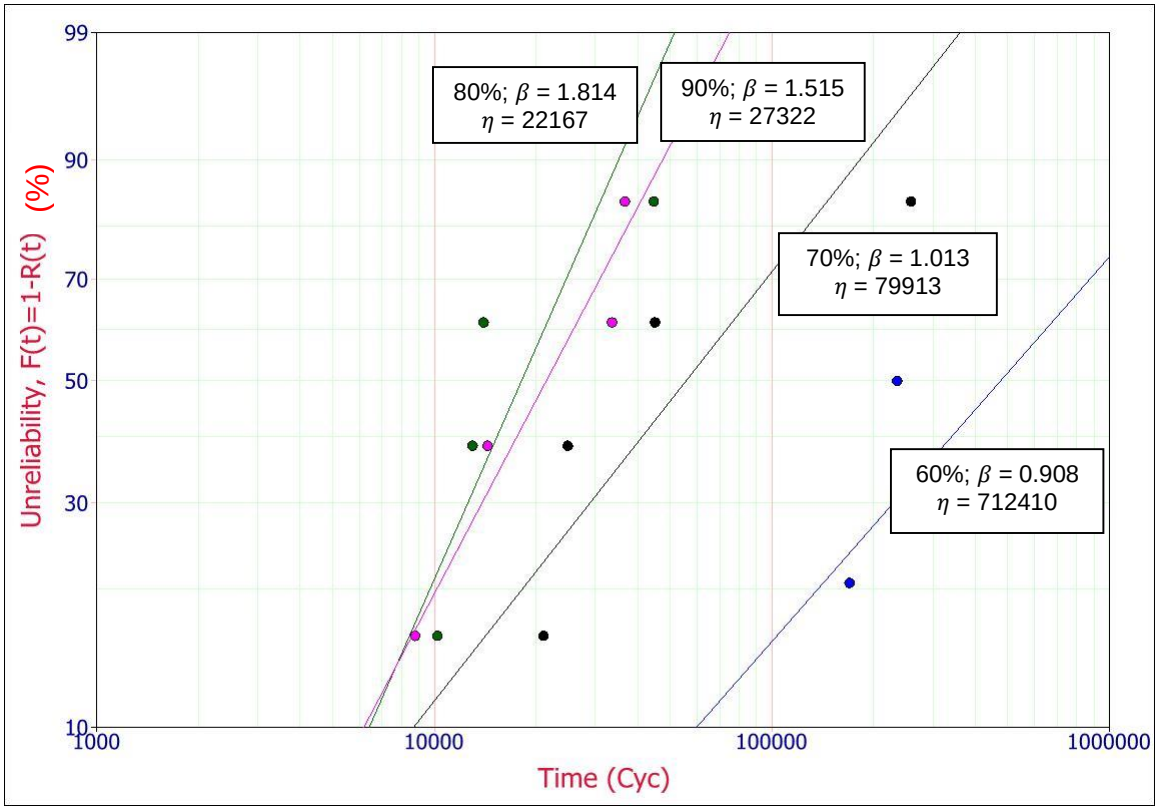

Figure 98 Weibull analysis of fatigue life data at various stress levels

The horizontal scale of Fig. 97 is the load in a logarithmic scale while it is the number of cycles to failure in Fig. 98. Both vertical scales are CDF or unreliability *F(X)* as described in Equation 21.

Reliability *R(X)* plots and CDF or unreliability *F(X)* plot are also shown in figures below:

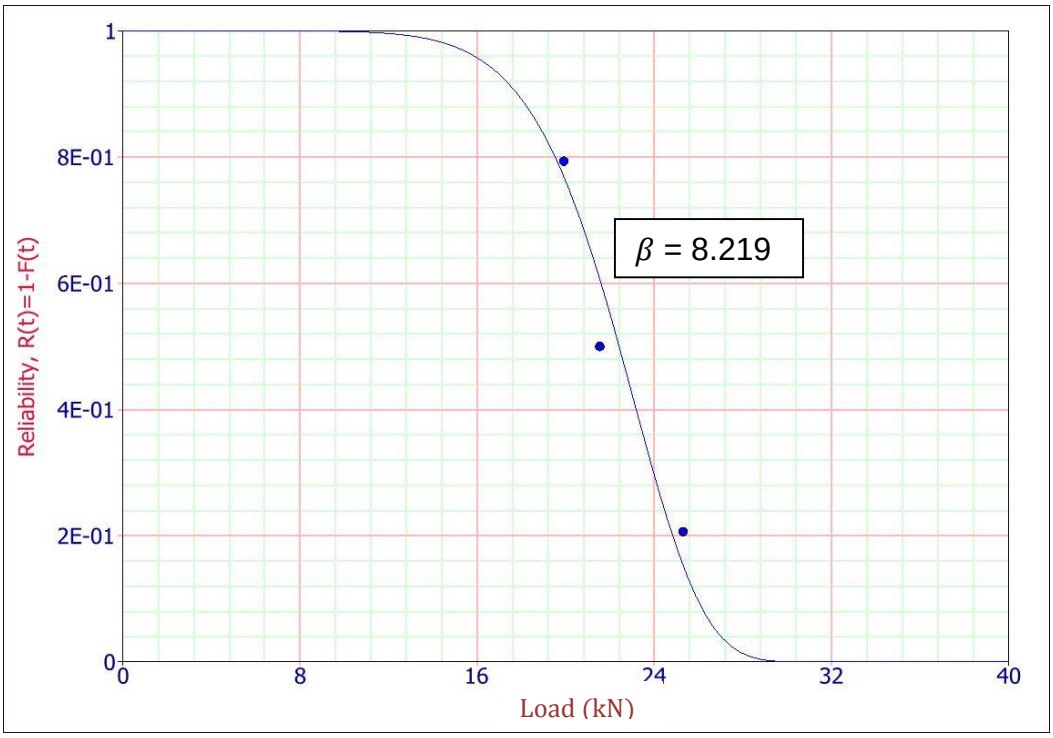

Figure 99 Reliability vs. load of static tests

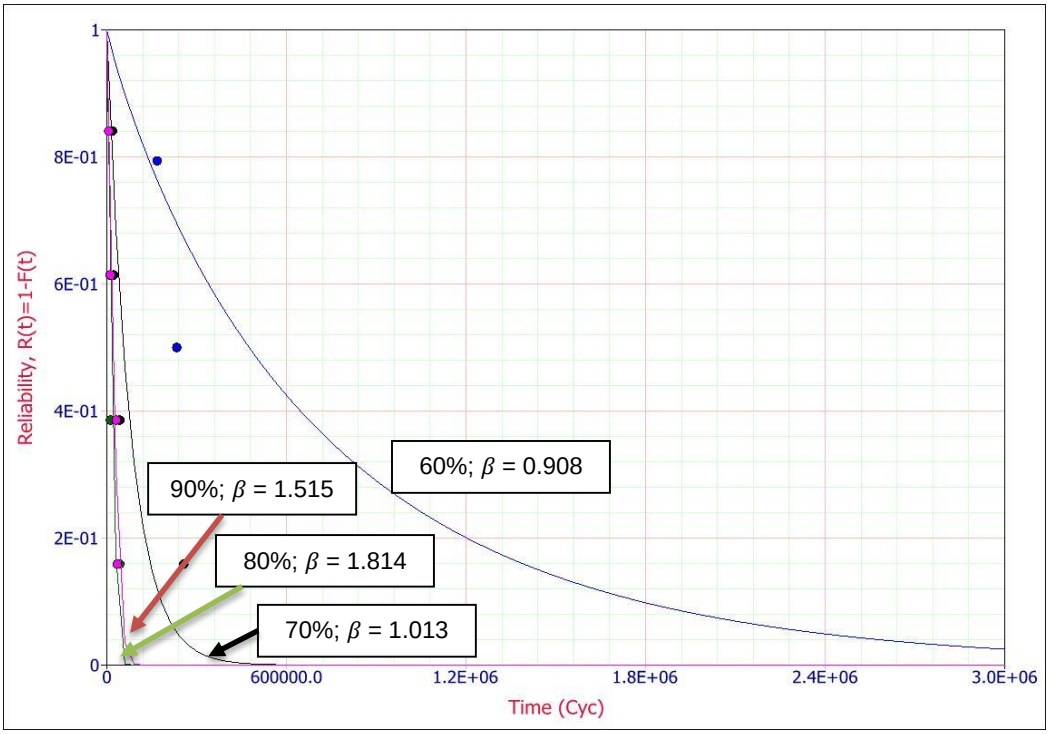

Figure 100 Reliability vs. number of cycles to failure of fatigue tests

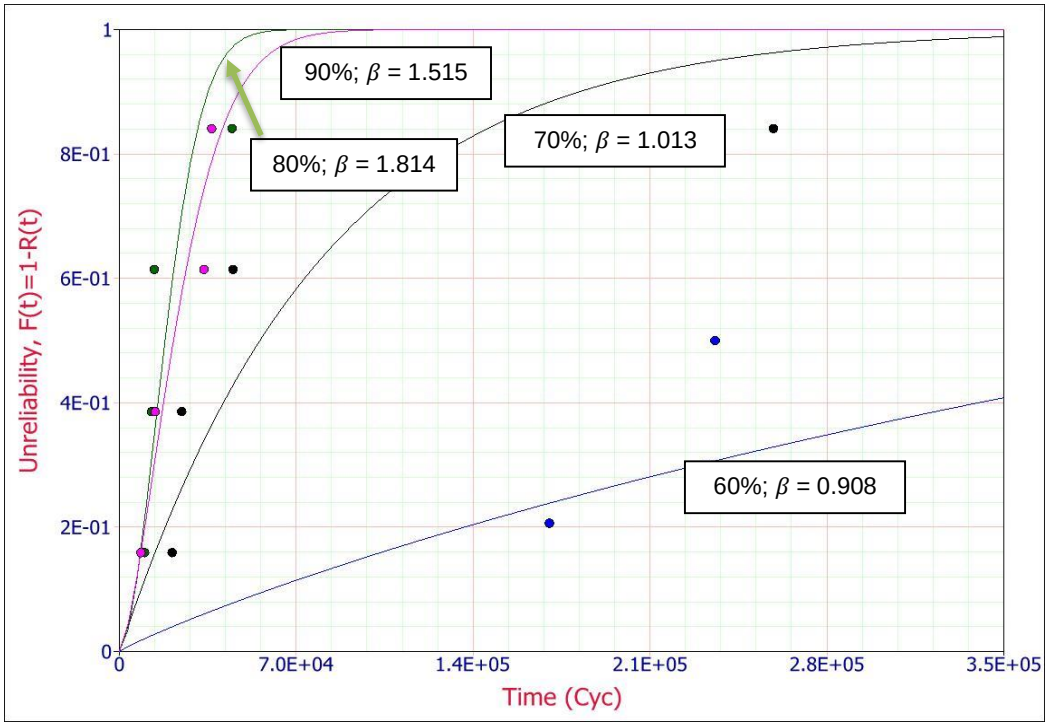

Figure 101 CDF vs. number of cycles to failure of fatigue tests

The horizontal scale of Fig. 99 is the load in a normal scale while it is the number of cycles to failure in Fig. 100 and 101. Fig. 101 is plotted with a more magnified X-axis than Fig. 100 to illustrate clearly all the data points. Both vertical scales of Fig. 99 and 100 are reliability function as described in Equation 20. Vertical scale of Fig.101 is CDF or unreliability function as described in Equation 21.

Several observations can be drawn from Table 13, Fig. 97 through 101:

1. The shape parameters of fatigue test data are considerably lower than that of static test data. This signifies that the fatigue failure process is more uncertain than static failure modes. This can be confirmed by comparing Fig. 97 and 98. The notch fabrication process that has been performed on WS samples may very possibly be the main reason of this uncertain failure mode;

2. Shape parameters have the trend to decrease as the load or stress level decreases. This indicates that more uncertainty happened in lower stress level during the fatigue testing;
3. Reliability decreases as number of cycles increases. This means more of the population will fail when more cycles are applied on sample;
4. The shape of reliability functions of fatigue test data is different from that of static test data (Fig. 99 and 100). R(X) of fatigue test data has a sharp decrease in the beginning while R(X) of static test data has a much smaller decrease in the beginning;
5. In Fig. 100, it is observed that the R(X) of 90 and 80%P_{ult} are almost the same, while the other two R(X) have much smaller slopes. This means that the reliability of WS samples of 90 and 80%P_{ult} decreases more quickly than WS samples of 70 and 60%P_{ult} while subjected to the increase of number of fatigue cycles.
6. The tuning problem that caused compression was proved to be minimal by Weibull analysis. The fatigue machine was tuned for all samples of 60%P_{ult}. And each of the previous load/stress levels included a sample that was tested after the tuning (refer to Table 9 for these samples). It can be observed in Table 13 that the shape parameter of 60%P_{ult} is smaller than that of other stress levels. This means that the tuning didn't make the data less scattered. Therefore, the tuning problem had a minimal effect on the fatigue data.

6. DISCUSSION AND CONCLUSION

A method of notch creation by anodic dissolution process was developed in this thesis study. Studies on corrosion are usually time consuming. In this thesis study, a strong current and a large volume of electrolyte largely enhanced the metal dissolution rate, which made the study possible in a short amount of time. Weight loss and remaining thickness measurement (Table 3 and 4) suggested that the dissolution processes were consistent on WS samples. This consistency was guaranteed by control on the current, the corroding time and the position of anode and cathode. Although corrosion processes were consistent, the shape of notches varied from each other. Especially the notch depth varied along the breadth. This was very possibly the main reason of scattered fatigue data despite the uncertainty of fatigue tests. However, this variation was reasonable considering the nature of uncertainty of corrosion.

Experiments of only one set of corrosion parameters (current and corroding time) were carried out in this thesis study. Further studies should perform more variations that could result in different shapes and dimensions of the notch.

During the fatigue testing on corrosion notched WS samples, cracks initiated and propagated in the notch as expected. These cracks initiated from the edge where the notch was the deepest. The stress concentration was most severe at these

locations. Typical three stages of fracture were confirmed with SEM fractographs. Both ductile and brittle fracture modes were found on failed specimens. Fatigue striations were observed for samples of all load/stress levels. Each of these striations was the result of a single fatigue cycle.

It was noticed that in the S-N diagram (Fig. 96), the mean number of cycles to failure of 80%Pult is a little smaller than that of 90%Pult. Two reasons should have caused this: the variation of notch shape from sample to sample; the tuning problem which caused compression on samples during fatigue cycles. However, this tuning problem was proved to have minimal effects by Weibull analysis.

Fatigue notch factor calculated from S-N diagram indicates that the fatigue strength of A606-04 Type 4 weathering steel is between AASHTO Category B and C^* after being corrosion notched. In addition, there is a decrease of fatigue strength of 34.49% compared to category A rolled beam.

Weibull analysis indicates that lower load/stress levels have generated more scattered data and the reliability of higher load/stress levels decrease more quickly as number of cycles to failure increases.

Samples were tested by tensile fatigue tests in this thesis study. Further studies should perform bending fatigue tests which simulates better the loading on WS I-beams.

7. REFERENCES

[1] Albrecht, P., Naeemi, A.H., “Performance of Weathering Steel in Bridges.” NCHRP Rep. No. 272. Transportation Research Board, Washington, D.C., 1984.

[2] Nickerson, R.L., “Performance of Weathering Steel in Highway Bridges.” A third phase report. American Iron and Steel Institute, Washington, D.C., pp.3, 1995.

[3] Virmani, Y.P., “TECHBRIEF Improved Corrosion-Resistant Steel for Highway Bridge Construction Knowledge-Based Design.” FHWA Publication No.: FHWA HRT-09-053, U.S. Department of Transportation, Aug. 2009.

[4] Granata, R.D., Wilson, J.C., Fisher, J.W., “Assessing Corrosion on Steel Structures Using Corrosion Coulometer.” Journal of Infrastructure Systems, pp.139-144, Sep. 1996.

[5] Revie, R.W., Uhlig, H.H., “Corrosion and Corrosion Control-An introduction to Corrosion Science and Engineering.” 4th Edition, Wiley Interscience, 2008.

[6] ASTM, “Standard Practice for Preparing, Cleaning, and Evaluating Corrosion Test Specimens.” ASTM G1-03.

[7] Garcia, D.B., Forman, R., Shindo, D., “Experimental evaluation of fatigue crack initiation from corroded hemispherical notches in aerospace structural materials.” Fatigue & Fracture of Engineering Materials & Structures, 35, pp.122-140, 2011.

[8] Wagner, C., “Corrosion Science.” 5, pp.751, 1965.

[9] Albrecht, P., Shabshab C.F., Li, W., Wright, W., “Remaining fatigue strength of corroded steel beams.” International Association for Bridge and Structural Engineering Workshop, Vol. 59, pp.71-84, 1990.

[10] Albrecht, P., “SEM Characterization of Naturally and Artificially Weathered A588 Steel.” Scanning Electron Microscopy, Vol. 1, pp.719-724, IIT Research Institute, Chicago, Illinois, Mar. 1977.

[11] Albrecht, P., Shabshab, C., “Fatigue Strength of Weathered Rolled Beam Made of A588 Steel.” J. Mater. Civ. Eng., p407-428, 1994.

[12] Albrecht, P., Lenwari, A., “Fatigue Strength of Weathered A588 Steel Beams.” J. Bridge. Eng., p436-443, 2009.

[13] James, P.H., Kao-Wen, M., Augustine, J.W., “The Electrochemical Machining of Mild Steel in $NaBrO_3$ Solutions.” Corrosion Science, Vol. 12, pp.571-578, Pergamon Press, 1972.

[14] Mahfuz, H., Maniruzzaman Md., Vaidya, U., Brown, T., Jeelani, S., “Response of SiC_f/Si_3N_4 Composites under Static and Cyclic Loading – An Experimental and Statistical Analysis.” Transactions of the ASME, Vol. 119, pp.186-193, Apr. 1997.